

A Bayesian hierarchical model to estimate land surface phenology parameters with harmonized Landsat 8 and Sentinel-2 images

Chad Babcock^{a,*}, Andrew O. Finley^b, Nathaniel Looker^c

^a*University of Minnesota, Department of Forest Resources, St. Paul, MN, 55108, USA*

^b*Michigan State University, Forestry Department, East Lansing, MI, 48824, USA*

^c*University of Minnesota, Department of Soil, Water and Climate, St. Paul, MN, 55108, USA*

Abstract

We develop a Bayesian Land Surface Phenology (LSP) model and examine its performance using Enhanced Vegetation Index (EVI) observations derived from the Harmonized Landsat Sentinel-2 (HLS) dataset. Building on previous work, we propose a double logistic function that, once couched within a Bayesian model, yields posterior distributions for all LSP parameters. We assess the efficacy of the Normal, Truncated Normal, and Beta likelihoods to deliver robust LSP parameter estimates. Two case studies are presented and used to explore aspects of the proposed model. The first, conducted over forested pixels within a HLS tile, explores choice of likelihood and space-time varying HLS data availability for long-term average LSP parameter point and uncertainty estimation. The second, conducted on a small area of interest within the HLS tile on an annual time-step, further examines the impact of sample size and choice of likelihood on LSP parameter estimates. Results indicate that while the Truncated Normal and Beta likelihoods are theoretically preferable when the vegetation index is bounded, all three likelihoods performed similarly when the number of index observations is sufficiently large and values are not near the index bounds. Both case studies demonstrate how pixel-level LSP parameter posterior distributions can be used to propagate uncertainty through subsequent analysis. As a companion to this article, we provide an open-source Rpackage **rsBayes** and supplementary data and code used to reproduce the analysis results. The proposed model specification and software implementation delivers computationally efficient, statistically robust, and inferentially rich LSP parameter posterior distributions at the pixel-level across massive raster time series datasets.

Keywords: land surface phenology, remote sensing, Bayesian hierarchical model, phenology, enhanced vegetation index, time series

1. Introduction

From spring budbreak through winter dormancy, temperate forest vegetation changes seasonally. The timing and magnitude of the phenological events that indicate transitions in vegetation behavior are primarily driven by temperature and water availability (Aber & Melillo, 2001). The vegetation phenology cycle shifts with changes in climatic variables, such as seasonal average temperatures and precipitation (Jeong et al., 2011). This makes tracking changes in vegetation phenology important for understanding how climate change will impact terrestrial ecosystems (Parmesan & Yohe, 2003). Improving climate model projections and monitoring ecosystem response to climate change require spatially and temporally accurate information about vegetation phenology (Piao et al., 2019). This need continues to motivate research activities aimed at collecting data and developing methods to provide high-quality spatio-temporal phenology information (Morisette et al., 2009).

Monitoring seasonal changes in vegetation using using imagery, i.e., land surface phenology (LSP), has a long history in remote sensing (Zeng et al., 2020). Exploring the use of early satellite remote sensing

*Corresponding author

systems, such as the Advanced Very High Resolution Radiometer (AVHRR) and Landsat Multispectral Scanner (MSS), to estimate LSP parameters started in the 1970s (Rea & Ashley, 1976; Goward et al., 1985; Taylor et al., 1985). These early studies showed images from satellites could be used to effectively estimate many phenological parameters for both natural and cultivated landscapes (Henderson & Badhwar, 1984; Spanner et al., 1990); however, low spatial and temporal resolution of early remote sensing datasets limited LSP parameter mapping at fine scales.

The launch of the Moderate Resolution Imaging Spectroradiometer (MODIS) in 2000 ushered in a new wave of LSP research. These studies aimed to exploit the high temporal resolution reflectance data products MODIS continues to offer (Ahl et al., 2006; Zhang et al., 2003; Ganguly et al., 2010). Currently, the United States National Aeronautics and Space Administration (NASA) hosts the MODIS Land Cover Dynamics product (MCD12Q2 C6) that provides annual LSP parameter estimates at a 500 m spatial resolution for the globe from 2001 to present (Sulla-Menashe et al., 2019). In 2011, the Visible Infrared Imaging Radiometer Suite (VIIRS) was launched. This sensor system was designed as a replacement to the aging MODIS Aqua and Terra satellites. NASA also hosts the VIIRS Global Land Surface Phenology Product (VNP22Q2) that provides annual 500 m resolution LSP parameters from 2013 through 2018 (Zhang et al., 2018).

Over the past decade, remote sensing technology has advanced tremendously and, with it, the ability to collect imagery useful for higher spatial resolution LSP parameter estimation (Melaas et al., 2013; An et al., 2018). NASA’s Landsat 8 and the European Space Agency’s (ESA) Sentinel-2 A and B satellites now collect and make publicly available reflectance data for the entire globe at unprecedented spatial, temporal, and radiometric resolutions. Combined, Landsat 8 and Sentinel-2 provide global coverage imagery at a nearly 3 day repeat interval (Li & Roy, 2017). The Harmonized Landsat Sentinel-2 (HLS) project is an effort by NASA to bring Landsat 8 Operational Land Imager (OLI) and Sentinel-2 Multispectral Instrument (MSI) reflectance data together (Claverie et al., 2018). The HLS product is produced using processing steps designed so researchers can combine OLI and MSI surface reflectance images seamlessly into a single time series for analysis. With the HLS dataset, the remote sensing and geospatial analysis community has access to analysis-ready imagery that is temporally dense enough to potentially estimate LSP parameters at 30 m resolution annually (Bolton et al., 2020; Kowalski et al., 2020).

Along with improvements to remote sensing data collection, there have been methodological advancements for translating reflectance readings into meaningful LSP parameters. Vorobiova & Chernov (2017) and Zeng et al. (2020) provide an extensive survey of approaches used to extract LSP parameters from vegetation index (VI) time series. We focus our attention on the double logistic curve fitting technique (Zhang et al., 2003; Elmore et al., 2012; Melaas et al., 2013). The approach generally involves fitting separate spring and autumn logistic functions to a VI time series for a pixel using a nonlinear model fitting algorithm. The spring function models VI behavior from winter dormancy to the midsummer growing season, and the autumn logistic function models VI behavior from midsummer back to dormancy. To determine the day of year (DOY) transition date from spring to autumn functions, Melaas et al. (2013) calculated slopes for moving windows across the time series. The earliest (after DOY = 90) detection of a negative slope in a moving window was set as the transition DOY for the pixel. One of the key strengths to the phenology curve fitting approach is the spring and autumn function coefficients can be meaningfully interpreted as LSP parameters (Melaas et al., 2013; Elmore et al., 2012). Many other approaches require further manipulation of the fitted curve to derive ecologically relevant metrics (e.g., derivatives to find inflection points, minimums, and maximums). The logistic function approach is also well constrained to ensure sensible phenology curve fits. Many spline fitting algorithms have a tendency to over-fit noisy data, leading to multiple peaks and valleys that are likely artifacts of data noise rather than true phenological signal.

Building upon Melaas et al. (2013), Senf et al. (2017) placed the spring logistic function in a Bayesian model to estimate the LSP parameters and demonstrate the usefulness of this statistical paradigm for quantifying parameter uncertainty. Senf et al. (2017), however, left for future research the derivation of a single Bayesian LSP model capable of fitting both spring and autumn functions and development of model fitting algorithms able to feasibly deliver Bayesian inference on more than a few hundred pixels. Our work aims to address both of these points.

The overarching objective of this paper is to advance model development work detailed in Melaas et al. (2013) and Senf et al. (2017). Specifically, we propose an approach to simultaneously estimate spring and

autumn logistic function parameters for a VI time series within a single Bayesian model. Casting these functions in a single Bayesian model allows the entire phenology curve to be estimated with statistical rigor and yields full uncertainty quantification for LSP parameters. Additionally, we developed an open-source Rpackage **rsBayes** (Finley & Babcock, 2020) that provides functions for efficiently sampling from the proposed LSP model parameters’ posterior distributions using a Markov chain Monte Carlo (MCMC) algorithm. The proposed LSP model’s ability to deliver robust LSP parameter estimates is assessed using two case studies. The case studies consider an Enhanced Vegetation Index (EVI) time series for cloud-free forested pixels within a HLS tile. In the first case study, we pool EVI time series across years (2013-2019) to estimate long-term average LSP curves as was done in Fisher et al. (2006) and Elmore et al. (2012). We examine how EVI observation sample size and data variability contribute to LSP parameter uncertainty at the pixel level. In the second case study, we fit the proposed LSP model using annual EVI observations to assess reliability of LSP parameter estimates given differing sample sizes. Using an abbreviated forest change detection analysis, this case study also demonstrates how the proposed error propagation approach is useful for estimating the posterior distribution of new parameters computed from the LSP model’s parameters.

Supplementary material includes the data and software needed to reproduce our results and additional Rfunctions that facilitate efficient fitting of the proposed model over massive pixel arrays (e.g., entire Sentinel-2 tiles) for multi-core processor computer systems. We conclude by discussing potential ways to further improve the proposed Bayesian LSP approach through model refinement and increased posterior sampling efficiency.

2. Model development

2.1. Land surface phenology function

We develop a LSP function by building on the approaches outlined in Melaas et al. (2013) and Senf et al. (2017). Here, for a given spatial location, e.g., pixel, we denote $y(t)$ as the observed VI at time t . As in Melaas et al. (2013), the first order behavior of y over a year, i.e., $t = 1, 2, \dots, T$ with $T = 365$, can be modeled using two logistic functions. The spring function is

$$S(t) = \alpha_1 + \frac{\alpha_2 - \alpha_5 t}{1 + e^{-\alpha_3(t - \alpha_4)}}, \quad (1)$$

where α_1 is seasonal minimum greenness, α_2 is the seasonal amplitude, α_3 is the green-up rate, α_4 is the green-up inflection point, and α_5 controls the mid-growing season greenness trajectory. The autumn function is defined as

$$A(t) = \alpha_1 + \frac{\alpha_2 - \alpha_5 t}{1 + e^{-\alpha_6(\alpha_7 - t)}}, \quad (2)$$

where α_6 is the green-down rate and α_7 is the autumn inflection point. We propose the following step function to seamlessly combine (1) and (2),

$$G(t) = \begin{cases} S(t) & 1 \leq t \leq \delta \\ A(t) & \delta < t \leq 365 \end{cases}, \quad (3)$$

where δ is the time t where $S(t) = A(t)$ and is itself a random variable equal to $(\alpha_3\alpha_4 + \alpha_6\alpha_7)/(\alpha_3 + \alpha_6)$. This step function provides a smooth transition between the spring and autumn components and facilitates full uncertainty quantification for δ and those parameters that describe the transition between mid-season phenology stages, e.g., mid-growing season greenness trajectory α_5 . The function parameters are illustrated in Figure 1.

2.2. Bayesian model

VIs derived from remotely sensed data typically have bounded support, e.g., index values can range from -1 to 1, or perhaps 0 to 1. Most functions proposed to approximate the seasonal trend in greenness are explicitly designed to accommodate this bounded support, e.g., leading to the logistic forms of $S(t)$ and $A(t)$

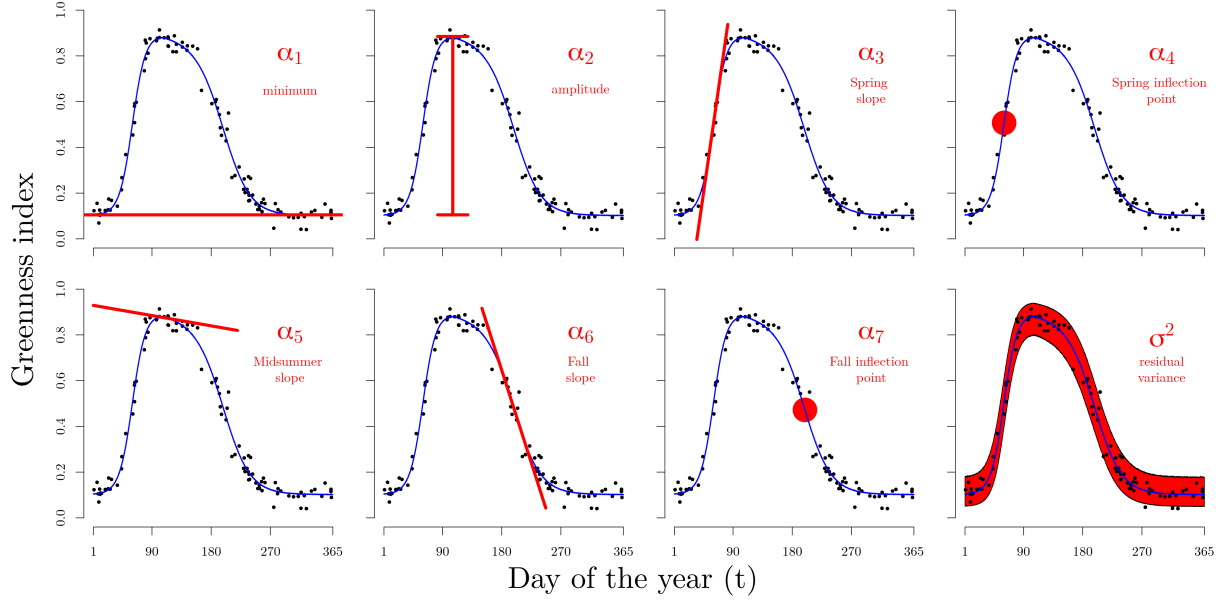


Figure 1: Graphic depictions of proposed LSP function (3) and Bayesian LSP model (4) parameters. α_1 is the LSP curve minimum. α_2 is the LSP curve amplitude. α_3 controls the spring side slope of the LSP curve. α_4 is the spring inflection point. α_5 controls the midsummer slope. α_6 controls the fall side slope of the LSP curve. α_7 is the fall inflection point. σ^2 models residual variance.

in Melaas et al. (2013) and our proposed $G(t)$. In such settings, the posited statistical model, within which $G(t)$ is couched, should also only be defined over the support of the VI. It is generally not desirable to use a statistical model that does not match the support of the response variable, as doing so can cause issues with parameter inference, uncertainty quantification, and subsequent prediction. In the current setting, such a mismatch occurs when a Normal likelihood is used to model a bounded VI as a response variable (this is the common approach used for model-based VI function fitting in the studies noted above). In this case, issues could arise because the Normal likelihood assumes the response variable and resulting model residuals can take any value on the whole real line—when in fact both the response and residuals are bounded. From a practical standpoint, applying a Normal likelihood here can inflate the estimated variance and generate fitted values and predictions outside the response variable’s support (Greene, 2008). A standard fix in these cases is to transform the response variable so that its support becomes the real line. The key drawback to this fix, however, is loss of model parameter interpretation with respect to the original response variable. Interpretation of these model parameters are key to many of the phenological characteristics of interest, so we would like to avoid transformation if possible.

We define a general Bayesian model that accommodates (3) for a variety of likelihoods with bounded and unbound support. The joint posterior distribution of the model’s parameters $\boldsymbol{\alpha} = (\alpha_1, \alpha_2, \dots, \alpha_7)^\top$ and likelihood variance σ^2 is

$$p(\boldsymbol{\alpha}, \sigma^2 | \mathbf{y}) \propto \prod_{t=1}^T \mathcal{L}(y(t) | G(t; \boldsymbol{\alpha}), \sigma^2, \cdot) \times \prod_{j=1}^7 U(\alpha_j | a_{\alpha_j}, b_{\alpha_j}) \times IG(\sigma^2 | a_{\sigma}, b_{\sigma}), \quad (4)$$

where $\mathbf{y} = (y(1), y(2), \dots, y(T))^\top$ is the vector of observed VI values, \mathcal{L} is the posited likelihood, $U(\cdot | a, b)$ is a Uniform prior distribution with lower and upper bounds a and b , respectively, and IG is an inverse-Gamma prior distribution with shape and scale hyperparameters a_{σ} and b_{σ} , respectively.

2.2.1. Candidate likelihoods

In the subsequent analyses we apply (4) using a Normal, Truncated Normal, and Beta likelihood. We denote the Normal likelihood as $\mathcal{L}_N(y(t) | G(t; \boldsymbol{\alpha}), \sigma^2)$. For values of $y(t)$ from a to b , the Truncated Normal is denoted $\mathcal{L}_{TN}(y(t) | G(t; \boldsymbol{\alpha}), \sigma^2, a, b)$. For values of $y(t)$ outside the interval $[a, b]$ the Truncated Normal likelihood equals 0, see, e.g., Hegde & Dahiya (1989) and Greene (2008) for more details. Lastly, we denote the Beta likelihood defined for values of $y(t)$ in the interval $(0, 1)$ as $\mathcal{L}_B(y(t) | G(t; \boldsymbol{\alpha}), \sigma^2)$. Smithson & Verkuilen (2006) offer a mild transformation that allows the response variable to assume values equal to 0 and 1, i.e., to accommodate the inclusive interval $[a, b]$ (although such a transformation is likely not needed in practice because values of exactly 0 and 1 are rare). Following Ferrari & Cribari-Neto (2004), we use the variate mean and a precision parameterization of the Beta likelihood where the precision is defined as $1/\sigma^2$.

2.2.2. Prior distributions

Given the somewhat complex nature of the non-linear function (3), some care is needed when selecting prior distributions to ensure: *i*) identifiability of model parameters; *ii*) sufficient flexibility to accommodate a variety of phenology curves; *iii*) meaningful quantification of uncertainty in parameter estimates. Selection of several prior distributions depends on the theoretical support of the VI, which we define as $\boldsymbol{\gamma} = (\gamma_1, \gamma_2)$ where the elements hold the lower and upper bounds, respectively. For example, EVI typically ranges from $\gamma_1 = 0$ to $\gamma_2 = 1$ in forested settings. As noted in (4), we use a Uniform prior distribution for each element in $\boldsymbol{\alpha}$. The seasonal minimum α_1 has prior support from γ_1 to γ_2 . We constrain the seasonal amplitude α_2 with support from 0 to $\gamma_2 - \alpha_1$. This prior upper-bound on α_2 ensures $\alpha_1 + \alpha_2$ does not exceed the VI's theoretical maximum γ_2 . Constraining α_3 and α_6 to support between 0 and 1 keeps estimated green-up and green-down rates within biologically sensible ranges. We ensure the spring inflection point α_4 occurs before the autumn inflection point α_7 , by setting its prior support from 0 to α_7 . We make explicit the assumption that the VIs are observed over a year by setting the support for α_7 from 1 to 365 (other ranges could be used).

For the midsummer slope parameter α_5 , one might constrain it to be between 0 and a small positive value, say 0.01, to capture the common slight decrease in midsummer greenness (note, given the parameterization of (1) and (2) a positive α_5 equates to a negative slope). Additional flexibility for slight midsummer greening can be accommodated by setting α_5 's prior to be bounded by values centered on 0, e.g., from -0.01 to 0.01. This would work as long as the sum of α_1 , α_2 , and additional greening captured by a negative α_5 does not exceed γ_2 . Of course this minor wrinkle could be solved by redefining the upper bound on α_2 , but we have not seen the need for this in practice, because rarely does $\alpha_1 + \alpha_2$ come close to γ_2 and there is rarely substantial midsummer greening. Finally, we prescribe σ^2 an inverse-Gamma $IG(a_\sigma, b_\sigma)$ with shape a_σ and scale b_σ . Given an $a_\sigma = 2$ this prior's mean is equal to b_σ and variance is infinite. A summary of the default prior distributions and hyperparameters used in the analyses presented in Section 3 are given in (5).

$$\begin{array}{llll} \alpha_1 \sim \mathcal{U}(\gamma_1, \gamma_2) & \alpha_3 \sim \mathcal{U}(0, 1) & \alpha_5 \sim \mathcal{U}(-0.01, 0.01) & \alpha_7 \sim \mathcal{U}(1, 365) \\ \alpha_2 \sim \mathcal{U}(0, \gamma_2 - \alpha_1) & \alpha_4 \sim \mathcal{U}(1, \alpha_7) & \alpha_6 \sim \mathcal{U}(0, 1) & \sigma^2 \sim IG(2, \cdot) \end{array} \quad (5)$$

2.3. Implementation and inference

Posterior inference about $\boldsymbol{\alpha}$ and σ^2 is based on MCMC samples that are generated using a Metropolis sampling algorithm (Gelman et al., 2013). With an aim to deliver inference for massive datasets comprising 10s of millions of pixels, we developed an MCMC algorithm and associated software tailored specifically to efficiently evaluate (4) with the flexibility to accommodate different candidate likelihoods and prior specifications. This work was implemented in **rsBayes**, an open source Rpackage that provides a function to generate the desired MCMC samples and a set of supporting utility functions for efficiently summarizing model parameters and other derived quantities of interest (Finley & Babcock, 2020).

A key advantage to using a Bayesian model is that we can sample the posterior distribution for any function of parameters in $\boldsymbol{\alpha}$ and σ^2 at each pixel (Gelman et al., 2013). Two posterior distributions of immediate interest are the model fitted and predicted values. A single sample from these, and other, derived posterior distributions is generated as output from the function of inferential interest given input of one

post-convergence joint posterior sample from (4). For example, to generate M samples from the posterior distribution of fitted values for observed time point t we use $\hat{y}(t)^l = G(t; \alpha^l)$ for $l = 1, 2, \dots, M$ where α^l is the l -th post-convergence sample of α . Similarly, to generate M samples from the posterior predictive distribution of a new time point t_0 , we draw $\hat{y}(t_0)^l$ as a random variate from the distribution corresponding to the likelihood used in (4), i.e., draws from a Normal, Truncated Normal, or Beta distribution with mean $G(t; \alpha^l)$ and variance $\sigma^{2,l}$.

Posterior distributions for other phenological characteristics of interest are generated in a similar fashion. For example, given M post-convergence MCMC samples of α , the corresponding M samples of season length, say $\lambda = \alpha_7 - \alpha_4$, are obtained one-for-one $\lambda^l = \alpha_7^l - \alpha_4^l$ for $l = 1, 2, \dots, M$. This inferential approach extends to more complex functions involving α . For example, say we would like to estimate the posterior distribution for the area under the phenology curve (AUC) over some time interval from t_1 to t_2 and denote this area as Φ . Again, the machinery is the same, we generate M samples from Φ 's posterior by evaluating $\Phi^l = \int_{t_1}^{t_2} G(t; \alpha^l) dt$ for each of $l = 1, 2, \dots, M$ posterior samples from α . Given the form of the integrand function G we could employ any number of numerical quadrature methods to estimate the area. This mechanism for estimating posterior distributions for parameters derived from α offers some exciting opportunities to explore uncertainty/sensitivity of complex quantities, e.g., phenology curve characteristics derived via differential equations (Zhang et al., 2003) or output from ecosystem process models that ingest phenology information as MCMC samples.

Given M samples from the posterior of α , σ^2 , and functions of these parameters, point and interval summaries are easily computed (see, e.g., Gelman et al. (2013) for details). In the subsequent analyses we use the median, standard deviation, and 95% credible interval computed using M post-convergence samples as point and associated uncertainty estimates for a given pixel. Importantly, these posterior summaries can be generated for each pixel and used to map parameter and derived quantities of interest with associated uncertainty.

3. Analyses of forest phenology inferred from Harmonized Landsat Sentinel-2 (HLS) data

The proposed modeling approach efficacy was assessed by estimating and analyzing key LSP characteristics using multi-year and multi-pixel reflectance data from the HLS tile described in Section 3.1. The subsequent analyses consider the performance of the proposed phenology function (3) and estimation of its parameters using the Bayesian model (4). Posterior summaries for model parameters, along with derived quantities such as the maximum greenness and area under the phenology curve (AUC) were collected using the **pheno** function in the **rsBayes** Rpackage.

Two case studies are detailed in the subsequent sections. Section 3.2 offers an analysis that yields pixel-level posterior distributions for the proposed phenology function and error model variance parameters. Here, the phenology function is estimated using composite EVI data, i.e., combining EVI observations over available years to estimate long-term average LSP parameters (2013-2019). Point and dispersion summaries for the pixel-level posterior distributions are then presented as raster data layers and compared with 2016 National Land Cover Database (NLCD; Yang et al., 2018) forest categories. Section 3.3 offers an analysis of a small area within the larger tile. This analysis assesses the robustness of phenology function parameters estimated using a small number of EVI observations collected on an annual time-step. The analysis also explores the usefulness of these data and inferential approach to detect interannual phenology change.

A data subset and Rcode needed to reproduce key portions of the subsequent analyses is provided as Supplementary Material.

3.1. Data

The motivating dataset comprised all 30 m HLS reflectance data (the L30 and S30 products) from January 1, 2013 to December 31, 2019, for tile ID 18TYN (available via <https://hls.gsfc.nasa.gov/data>). The tile, delineated by the white box in Figure 2(a), is positioned in the northeastern United States. The HLS imagery temporal resolution is given in Figure 3 and shows sparse coverage from 2013 to 2016 when only Landsat 8 data are available. Then, with the addition of Sentinel-2 data, temporal resolution increases

from 2016 through 2019. Within the tile, the availability of EVI observations used in the subsequent analyses varies based on satellite orbital path and cloud cover as shown in Figure 3(a). A total of 8,698,531 forested pixels, as specified by 2016 NLCD codes 41, 42, and 43, collectively comprising 1,101,352,942 EVI observations (i.e., sum of the pixel values in Figure 3(a)) were retained for subsequent analyses.

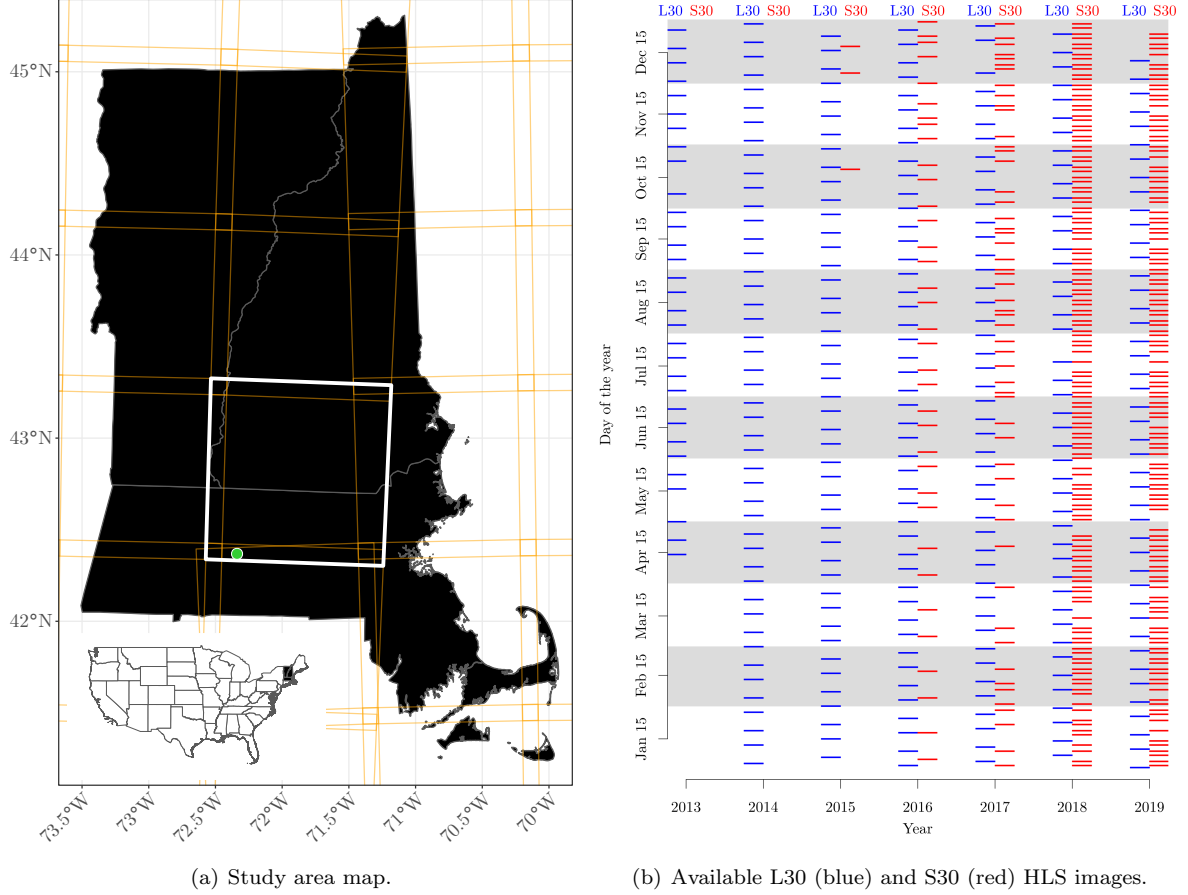


Figure 2: (a) White box delineates the Harmonized Landsat Sentinel-2 (HLS) study tile 18TYN analyzed in Section 3.2. The green point identifies the location of analysis in Section 3.3. (b) Availability of Landsat and Sentinel-2 data in the study tile delineated in Figure 2(a) over time.

3.2. Tile-wide composite long-term average LSP estimates and comparison with NLCD

The proposed phenology function (4) was fit using a Normal, Truncated Normal, and Beta likelihood to each pixel’s composite EVI observations within the study tile. Pooling the EVI data to produce a composite phenology curve is common practice when there is a paucity of observations within any given year (Fisher et al., 2006). Figure 4 illustrates composite EVI data for a typical pixel that remained forested over the seven year study period. Depending on the study objectives, pooling EVI observations across years might not be ideal, especially when there is large interannual variation in EVI values resulting from forest disturbance or other factors. Such settings have motivated work by Senf et al. (2017) who propose partial pooling by introducing a year random effect on select parameters in (1), (2), and similar LSP functions. While the addition of such random effects is beyond the scope of this study, it is a next logical step in the development and discussed further in Section 4.

As noted in Section 2, there is sound theoretical motivation to use a likelihood that matches the bounded support of the VI response variable, i.e., we would favor use of the Truncated Normal or Beta distribution to

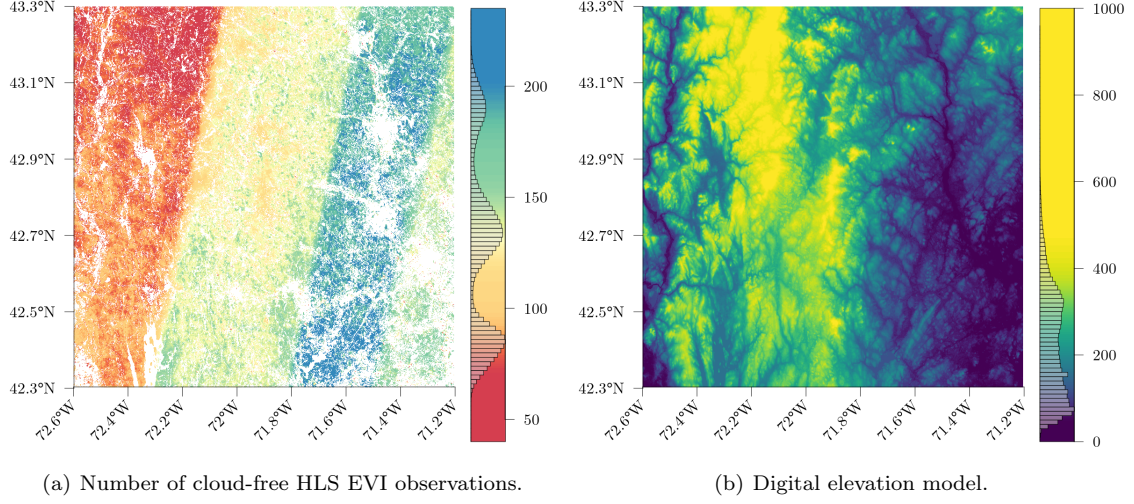


Figure 3: (a) Number of EVI observations at each 30 m pixel in the study tile. The histogram in the scale bar shows frequency of the given number of observations within the color range. (b) Digital elevation model derived from Shuttle Radar Topography Mission (SRTM) data for the study tile. Elevation units are meters.

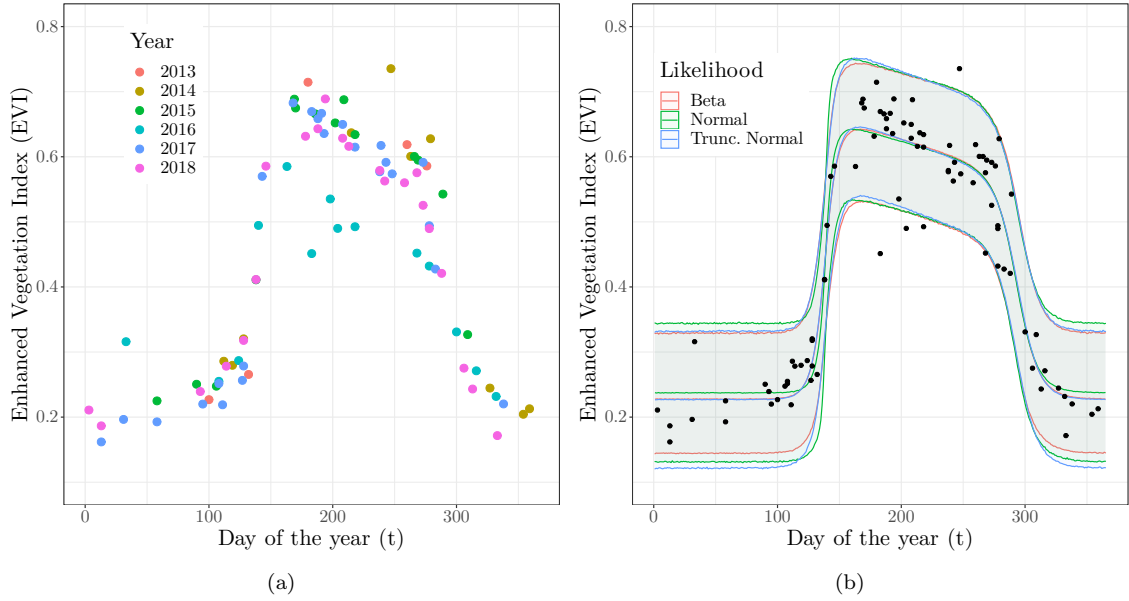


Figure 4: Example of composite Harmonized Landsat Sentinel-2 Enhanced Vegetation Index (EVI) time series for a continuously forested pixel. (a) EVI values by year. (b) Posterior predictive distribution median and 95% credible interval band for each of the three candidate likelihoods.

estimate the phenology function's parameters given EVI. However, for the composite EVI data considered here, the three likelihoods delivered highly comparable parameter estimates and fits to the observed data. As an example from one pixel, Figure 4(b) shows the posterior predictive distribution median and 95% credible interval bound for each likelihood. More broadly, Figure 5 illustrates the Pearson correlation between parameters estimated (posterior median) using the three likelihoods for all pixels in the study

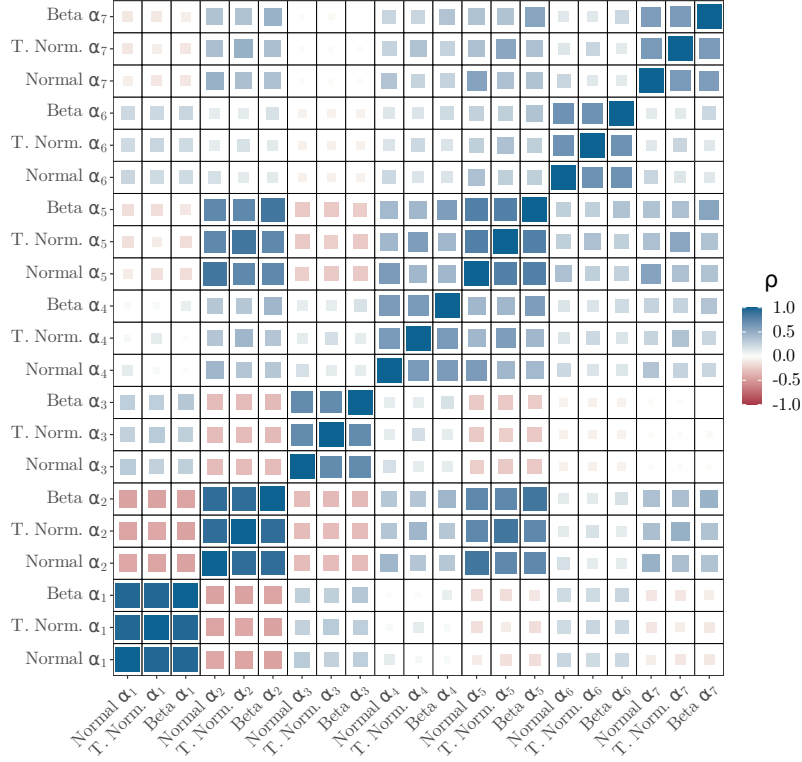


Figure 5: Person correlation (ρ) between phenology function (3) parameters estimated using (4) with the Normal, Truncated Normal (T. Norm.), and Beta likelihoods for all pixels in the study tile.

tile. It is evident from this figure that the choice of likelihood has negligible effect on the resulting point estimate for model parameters. Similarly, although not shown, the choice of likelihood has little effect on any given parameter's estimated posterior distribution shape and spread. As a result, there is essentially no difference between the predicted values generated at the observed time points among the three likelihoods—all three likelihoods yielded the same root mean squared error of 0.05 and nominal 95% posterior predictive distribution credible interval of 95.3. Despite the theoretical argument for using a bounded likelihood, these empirical findings are not surprising because EVI observations rarely have values close to the lower bound of 0 and upper bound of 1 in this dataset. If one considered data that frequently came up against the bounds, then inferential issues could arise if a Normal error model was assumed. Given the nearly indistinguishable results among the likelihoods, the remainder of the results presented in this section will be from the Beta regression model.

Figures 6 and 8 show composite (long-term average) α_1 , α_2 , α_4 and α_7 parameter estimates (posterior medians) and associated uncertainties (posterior standard deviations) generated using the Bayesian LSP model (with Beta likelihood) for the study tile. Corresponding maps for the remaining LSP parameters are provided as Supplementary Material. We see from the scale bar histogram in Figure 6(a) that α_1 (LSP curve minimum) tends to be between 0.2 and 0.3 with few estimates falling outside the range of 0.1 and 0.5. As seen in the scale bar histogram for α_2 (LSP curve amplitude) in Figure 6(c), the range of estimated LSP amplitudes spans from nearly 0 to 0.85 with an apparent average around 0.6. Shown in Figure 5, there is a moderate negative correlation between the α_1 and α_2 parameter estimates. Given the interpretation that α_1 is the LSP curve minimum and α_2 is its amplitude, we can reasonably expect forested pixels with lower minimum greenness to tend to have higher greenness amplitudes. This phenomenon may be related to the relative proportion of evergreen and deciduous vegetation in a pixel.

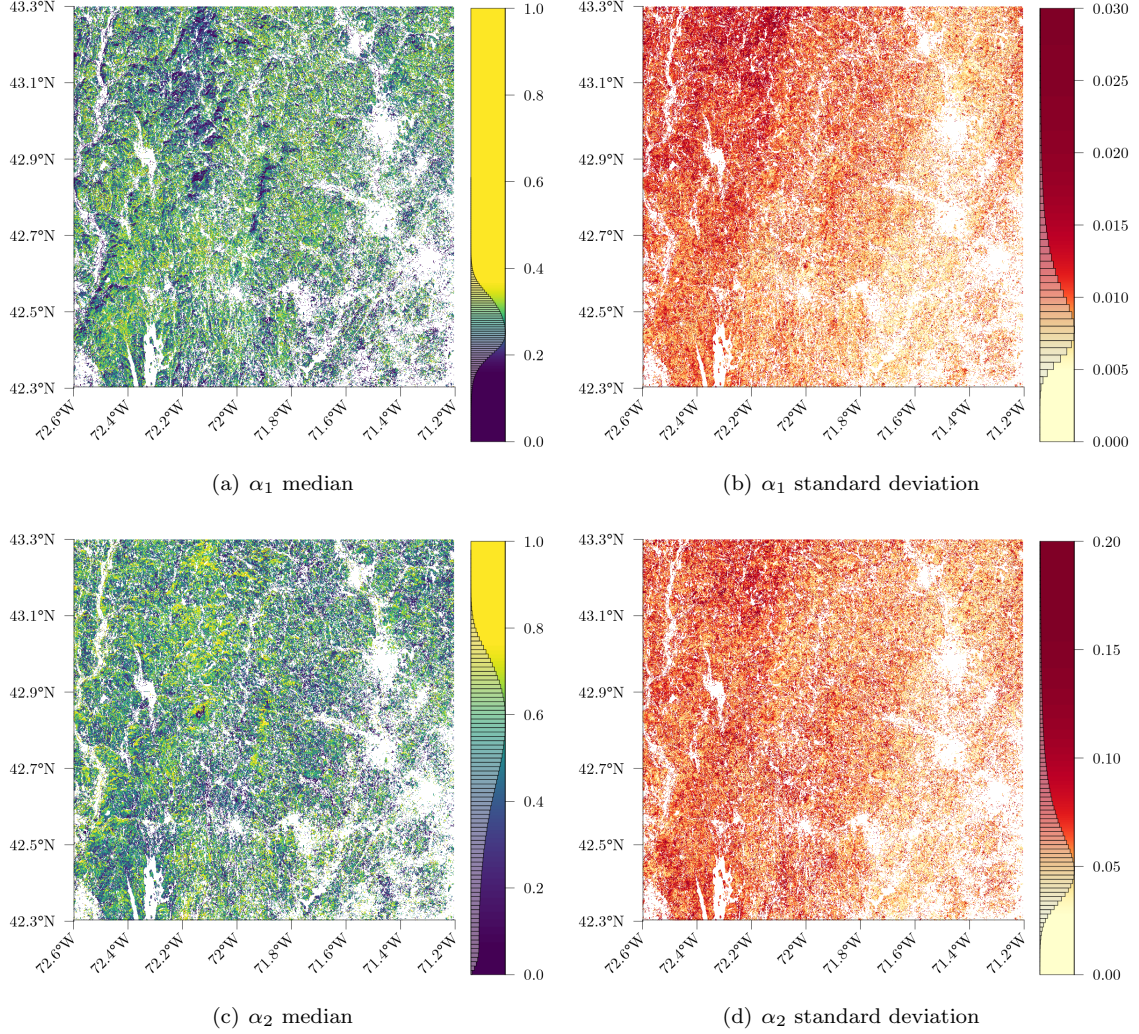


Figure 6: Maps showing spatial distribution of long-term average (2013-2019) minimum α_1 and amplitude α_2 and associated uncertainties estimated using the Bayesian LSP model.

Figure 7 shows histograms for α_1 , α_2 and $\alpha_1 + \alpha_2$ (LSP curve maximum) broken out by NLCD forest type code. Figure 7(a) shows a tendency for deciduous-class pixels to have lower seasonal minimums than mixed- and evergreen-class pixels. We also see in Figure 7(b) that deciduous-class pixels tend to have higher LSP curve amplitudes than the mixed and evergreen classes. This is a sensible result. We expect deciduous forests to have lower seasonal minimums than evergreen forests due to leaf shedding. Mixed and evergreen forests will tend to have higher EVI values in the dormant season because conifers retain needles year round. We see in Figure 7(c) that evergreen-class pixels tend to have lower LSP curve maximum estimates than mixed- and deciduous-class pixels. It is well-known that coniferous forests tend have lower summer EVI values than deciduous forests. It is encouraging to see this trend present in our LSP parameter estimates and indicates the moderate resolution LSP products using HLS data and our proposed modeling approach yield potentially insightful findings about forest phenology.

It is noticeable from Figures 6(b) and 6(d) that α_1 and α_2 uncertainties tend to vary with EVI observation sample size (comparing to Figure 3(a)). We see a tendency for higher posterior standard deviations in the north-west edge of the uncertainty maps. This is the region in the HLS tile with the fewest EVI observations

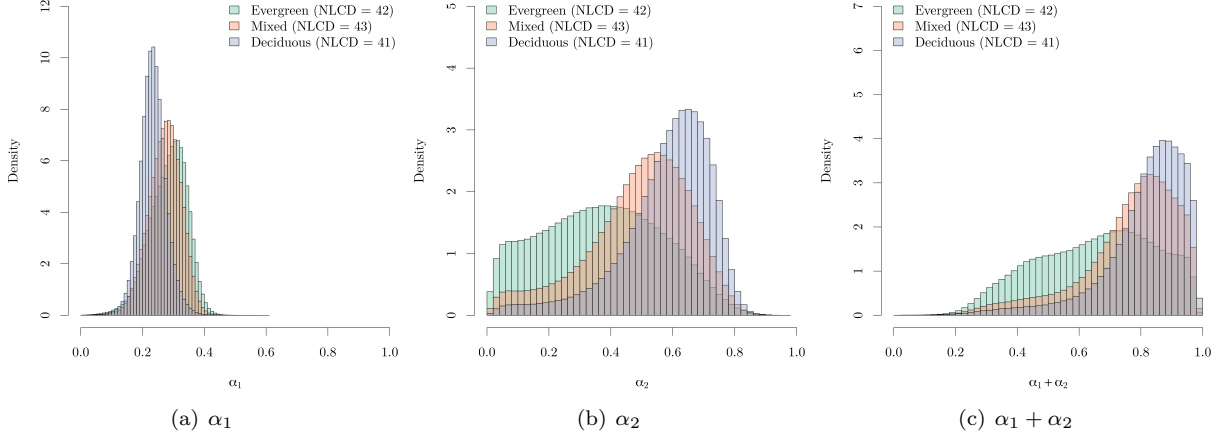


Figure 7: Histograms of composite (long-term average) α_1 , α_2 and $\alpha_1 + \alpha_2$ estimates (medians) by National Land Cover Database (NLCD) forest code.

per pixel, due to less sensor track swath overlap. It is even possible to make out borders where the amount of sensor path overlap changes across the tile by examining the spatial distribution of uncertainty in Figures 6(b) and 6(d). It is also apparent from the uncertainty maps that EVI observation sample size is not the only contributor to α_1 and α_2 uncertainty. As in any regression, parameter uncertainty is a function of sample size and the inherent variability of the data. Measures of posterior distribution dispersion, e.g., standard deviation, mapped to the pixels accounts for both sample size and data variability. Because the EVI sample size and variability is often pixel specific, it is important to provide pixel-level uncertainty assessment for LSP parameters.

In Figure 8(a) we see the start of growing season DOY (α_4) generally shifts from later in the year to earlier as we move from west to east. We also notice in Figure 8(c) the end of growing season DOY shifts (α_7) from earlier in the year to later from west to east. Comparing to Figure 3(b), it becomes clear that these trends are related to elevation. What these trends seem to show is the length of the growing season ($\alpha_7 - \alpha_4$) is inversely related to elevation. It is well understood that vegetation growing seasons tend to start later and end earlier in the year at higher altitudes. This general phenomenon seems to be reflected in the estimated LSP parameter maps.

3.3. Small area annual estimates and change detection

We again consider the phenology function (3) and estimation of its parameters using the three likelihoods within the Bayesian model (4), but unlike Section 3.2 we estimate models separately for each year. Using 2014, 2016, and 2018 National Agriculture Imagery Program (NAIP USGS, 2020) 1 m resolution imagery we identified forest areas that underwent substantial disturbance during the study period. Here, we highlight one such area of interest (AOI) identified by a green point in Figure 2(a). The 144 (21×21) 30 m HLS pixel AOI is on the Quabbin Reservoir Watershed System in central Massachusetts which is actively managed by the State's Department of Conservation and Recreation. Figure 9(a) shows 2014 NAIP imagery of the area which is dominated by an over-mature red pine (*Pinus resinosa*) plantation planted by the Civilian Conservation Corps in the 1940s. Management records provided by Beard (2020) indicate the area was thinned in 1991 and 1996. Since the 1996 harvest, black birch (*Betula lenta*) took over the understory and occupied about 20 to 30 square feet of basal area per acre by 2018. The residual mature red pine was killed by red pine scale (*Matsucoccus resinosa*) between 2014 and 2016, with mortality clearly visible in the center portion of the 2016 NAIP image in Figure 9(c). In early October 2018 a timber harvest was conducted to salvage the dead and dying red pine. The NAIP imagery shown in Figure 9(e) was taken within weeks of the harvest.

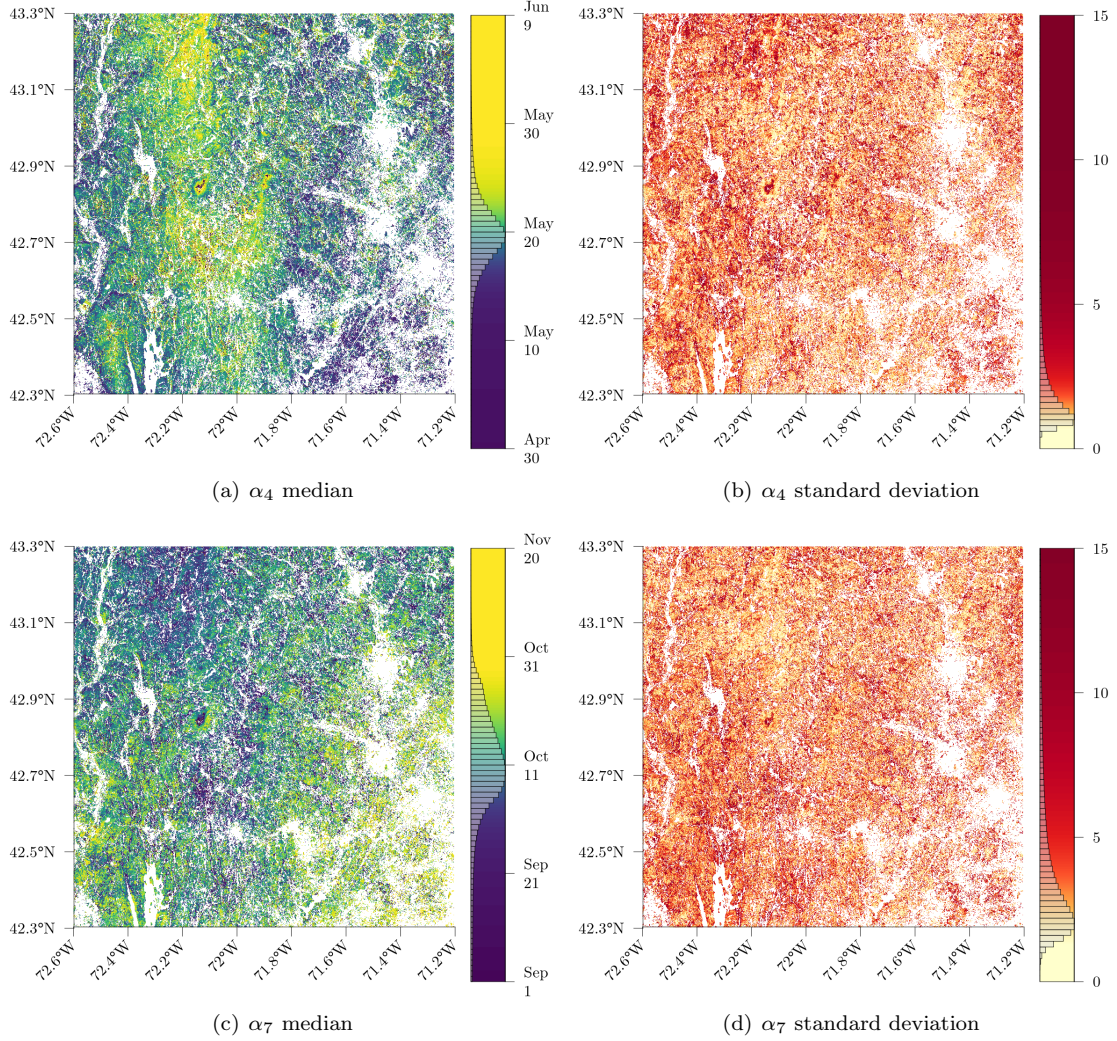


Figure 8: Maps showing spatial distribution of long-term average (2013-2019) α_4 and α_7 inflection points and associated uncertainties estimated using the Bayesian LSP model.

The AOI analysis has two parts. First, we consider EVI estimates for a short transect of six pixels delineated by the white box in Figure 9(a). Second, following the methods for sampling from Φ 's posterior distribution in Section 2.3, we estimate AUC as $\int_1^{365} G(t; \alpha) dt$ for each pixel in the AOI (see Supplementary Material for code implementation).

The six pixel transect was selected to illustrate LSP change from healthy forest in 2014 (Figure 9(a)) to partial forest (pixels 1-2) and partial harvest (pixels 3-6) in 2018 (Figure 9(e)). Figure 10 shows the posterior predictive median and 95% credible interval band for each likelihood fit to each transect pixels' annual EVI observations. As shown in Figure 3, the availability of HLS data increases over the study period. For years 2014-2019, EVI sample sizes for transect pixels range from 6-7, 11-12, 14-15, 12-13, 23-25, and 22-25, respectively. Increases in sample size results in narrowing of credible interval bands from 2014 to 2019 in Figure 10, with the most pronounced narrowing occurring between 2014 and 2016.

Looking at NAIP images in Figure 9, we can see transect pixels 3-6 are harvested in October 2018. In a non-leap year, October is days 274-304 which is well into the fall leaf senescence portion of the LSP curve for 2018 in Figure 10 and therefore we would not expect to observe a harvest effect on EVI estimates. However,

2019 mid-summer EVI credible interval bands estimated using the Beta and Truncated Normal likelihoods show clear separation between the non-harvested and harvested pixels. In comparison, the credible intervals estimated using the Normal likelihood are a bit wider and hence does not differentiate non-harvest and harvest pixels as clearly in 2019. In general, the Beta distribution provides marginally narrower credible intervals than the Normal and Truncated Normal likelihoods, while still maintaining a nominal credible interval coverage rate of 95% for observed EVI.

We turn now to the AOI AUC analysis. In general, there should be a positive association between greenness and LSP curve AUC. Following this idea, we would expect pre-harvest AUC to be greater than post-harvest AUC. Indeed, the harvested pixels in the 2018 NAIP image, Figure 9(e), have lower AUC estimates in Figure 9(f). While the AUC estimates identify harvest area, they do not seem to pick up the red pine mortality seen in the NAIP imagery prior to the harvest (i.e., comparing Figures 9(c) and 9(d)). For completeness, the AUC estimates for all years in the study period are given in Supplementary Figure S3.

With regard to pixel-level AUC uncertainty estimates, beyond approximately 12 EVI observations within a given year and pixel there is little change in the posterior distribution’s standard deviation. This can be seen when looking at Supplementary Figures S4 and S5, which map the AUC posterior standard deviation and sample size, respectively. The same general conclusion can be drawn looking at the credible interval band widths in Figure 10.

4. Discussion and conclusions

We propose a new approach to estimate LSP parameters using a Bayesian model that builds on work by Melaas et al. (2013) and Senf et al. (2017). We examined the Bayesian LSP model’s performance using EVI time series’ generated from HLS reflectance data. Composite long-term average LSP parameters were estimated for all NLCD forest class pixels in one HLS tile using three different likelihoods. We found there was negligible difference in parameter estimates from the different likelihoods indicating that, when VI sample size is sufficiently large and observed values are far from the VI’s bounds, a Normal likelihood can be used without compromised inference even though its support is not bounded. From a computational standpoint, evaluating the Normal likelihood is much faster relative to evaluating the Truncated Normal or Beta. This decreased computing time becomes especially important in a MCMC setting where the likelihood needs to be evaluated for each iteration in the sampler. This decrease in run time to deliver posterior samples from model parameters can lead to substantial compute time savings when larger datasets are considered, e.g., continental-scale analyses. As a point of reference, to deliver 15,000 post convergence MCMC samples for the ~ 7 million tile pixels run on a 64 core computer, the Beta likelihood took ~ 3 days whereas the Normal likelihood took ~ 2.5 days. However, in the AOI case study, we saw that when VI time series sample sizes are small, choosing the Beta or Truncated Normal likelihood delivered improved inference via narrower credible interval bands.

Examining LSP parameter estimates revealed relationships between NLCD forest type classes and LSP curve minimums, amplitudes, and maximums. The tendency for deciduous forests to have lower dormant season greenness, more significant spring green-ups, and higher maximum growing season greenness compared coniferous forests was clearly identified in the LSP parameter estimates. This result suggests that 30 m resolution LSP estimates from the Bayesian LSP model might be useful in ecological studies where vegetation phenology is thought to play a role.

We showed that disparity in sample size and inherent variability in LSP observations can impact LSP parameter estimates. Current and future large remote sensing time series datasets useful for LSP modeling, such as HLS, will have highly varying sample sizes and levels of data noise from pixel to pixel due to sensor path overlap and cloud cover among other factors. If we are going to use data like HLS to make LSP estimates, it will be important to obtain pixel-level uncertainties to identify when and where LSP estimates are made with sufficient certainty. It is common for LSP estimates to be used in downstream analyses. The MCMC sampling mechanism implemented here allows for easy propagation of LSP parameter estimate uncertainty in subsequent analyses. The uncertainty propagation process was demonstrated in our AUC calculations for the annual LSP curve estimation case study.

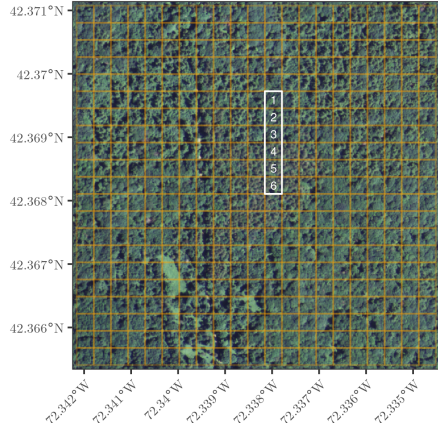
The Melaas et al. (2013) and Senf et al. (2017) studies provide a methodology to account for interannual variability when using VI observations pooled across years. We did not attempt to account for interannual variability in our first case study where pooled VI time series’ were used. This choice was largely influenced by computing time. While we have made significant attempts to speed up fitting times for the Bayesian LSP model, as with many MCMC based Bayesian model-fitting approaches, this model still requires substantial run time for even moderate sized datasets.

While not pursued here, our posited Bayesian model can accommodate random effects for LSP parameters to account for interannual variability with pooled data. We note that, considering the HLS dataset specifically, partial pooling models to account for interannual variability (as was used in Senf et al. (2017)) may not be necessary with post 2017 data (when OLI and both MSI sensors are fully operational). As seen in the second case study, LSP curves were estimated with sufficient certainty to track variation in LSP parameters from year-to-year for the selected individual pixels. Examining pixel-level uncertainties suggested that there is likely a sufficient number of observations each year so that pooling across years may not be needed to increase sample sizes.

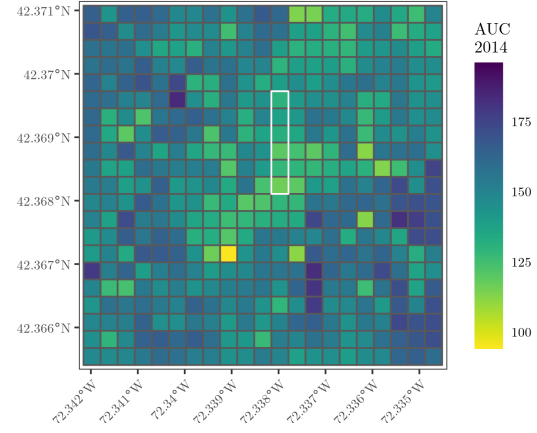
The Rpackage companion to the article, **rsBayes** (version 0.1.1), provides first-cut functionality for users to apply our Bayesian LSP approach to their own datasets. Considerable effort was made to develop efficient fitting algorithms written in C with an eye toward making this Bayesian LSP estimation approach viable for continental or global scale applications. As computing technology continues to improve at an exponential rate, we believe the modeling approach described here will be applicable at these scales in the near future.

Acknowledgments

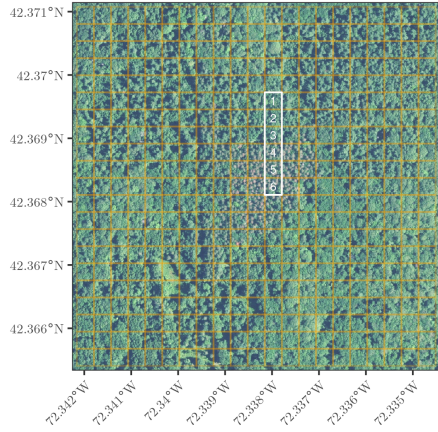
The work of the first and second author was supported, in part, by the USDA Forest Service Forest Inventory and Analysis (FIA) and Forest Health Monitoring (FHM) programs, and National Aeronautics and Space Administration’s Carbon Monitoring System project. The first author’s work was also supported through the Minnesota Agricultural Research, Education and Extension Tech Transfer program (AGREETT). The second author received additional support from the National Science Foundation (NSF) NSF/EF 1253225 and NSF/DMS 1916395. The third author’s work was supported by the NSF Graduate Research Fellowship and University of Minnesota Doctoral Dissertation Fellowship.



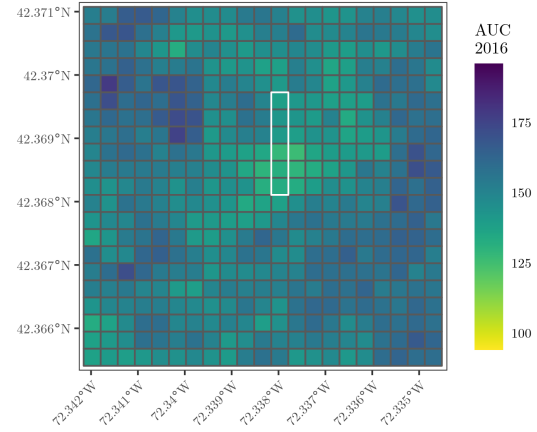
(a) NAIP July 21, 2014



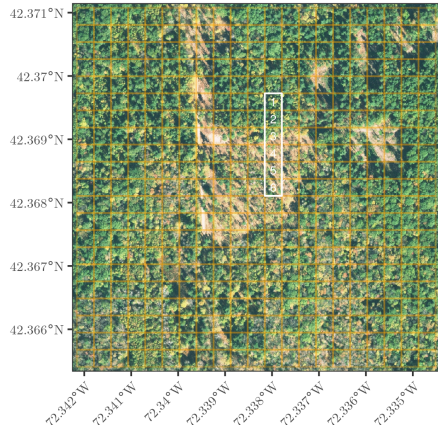
(b) Area under phenology curve, 2014



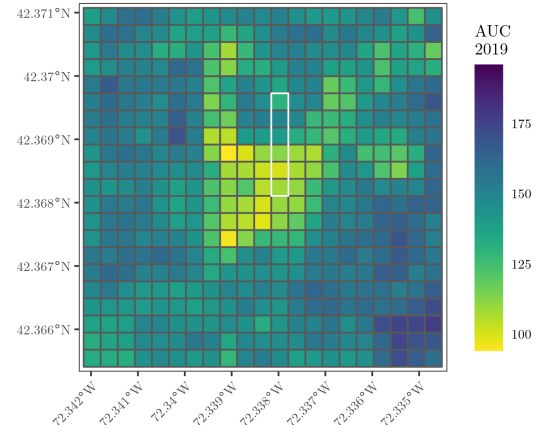
(c) NAIP August 7, 2016



(d) Area under phenology curve, 2016



(e) NAIP October 19, 2018



(f) Area under phenology curve, 2019

Figure 9: A 144 (21×21) 30 m HLS pixel area of interest on the Quabbin Reservoir Watershed System in central Massachusetts with broader geographic location identified with a green point in Figure 2(a). In the left column, HLS pixels are identified using an orange grid over NAIP imagery. The right column, pixel-level posterior distribution median estimate for the area under the phenology curve from the Beta likelihood model. The white rectangle delineates six pixels for which EVI observations and model results are illustrated in Figure 10.

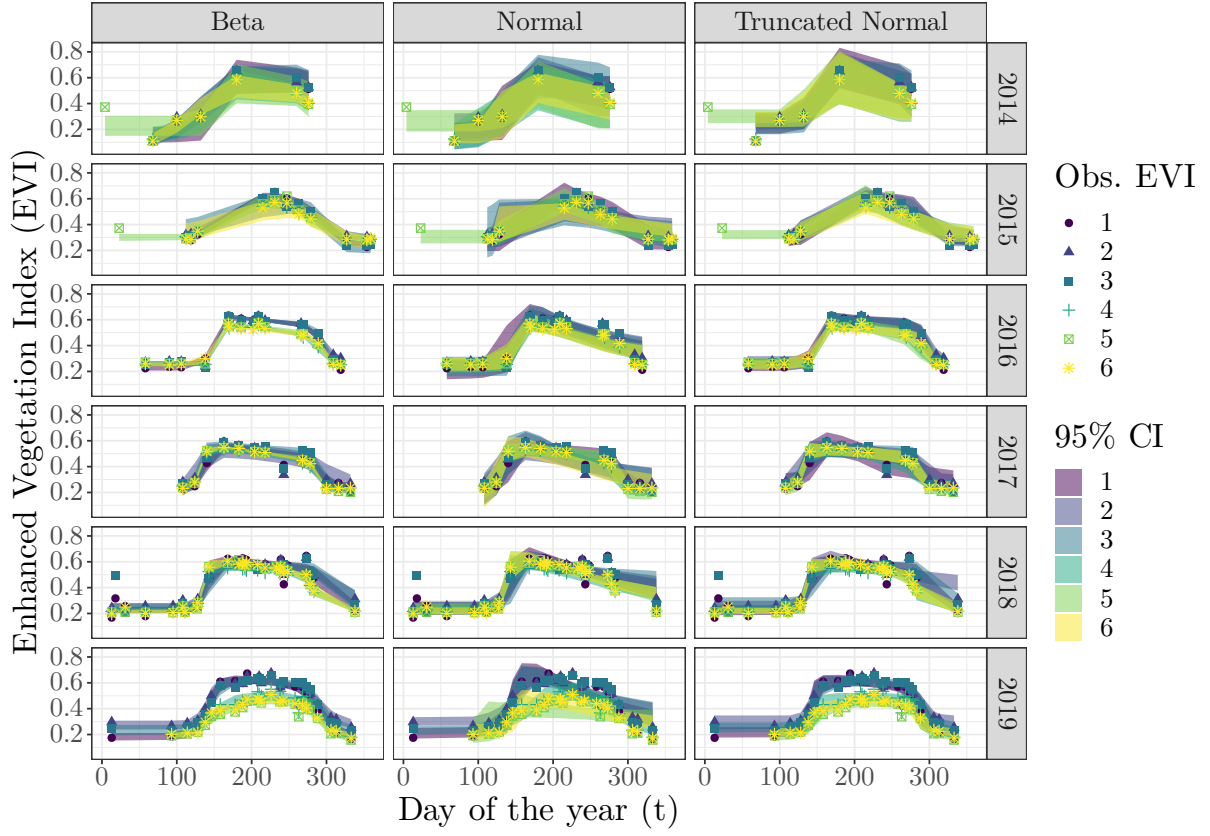


Figure 10: Model (4) fitted 95% credible interval (CI) bands for the Beta, Normal, and Truncated Normal likelihoods fit to annual EVI observations from the six pixels identified by the white box and corresponding number labels in Figures 9(a) (a).

References

- Aber, J., & Melillo, J. (2001). *Terrestrial Ecosystems*. 2 ed., Harcourt Academic Press, Burlington, MA.
- Ahl, D.E., Gower, S.T., Burrows, S.N., Shabanov, N.V., Myneni, R.B., & Knyazikhin, Y. (2006). Monitoring spring canopy phenology of a deciduous broadleaf forest using MODIS. *Remote Sensing of Environment*, 104, 88 – 95.
- An, S., Zhang, X., Chen, X., Yan, D., & Henebry, G. (2018). An Exploration of Terrain Effects on Land Surface Phenology across the QinghaiTibet Plateau Using Landsat ETM+ and OLI Data. *Remote Sensing*, 10, 1069.
- Beard, D. (2020). Private Communication.
- Bolton, D.K., Gray, J.M., Melaas, E.K., Moon, M., Eklundh, L., & Friedl, M.A. (2020). Continental-scale land surface phenology from harmonized Landsat 8 and Sentinel-2 imagery. *Remote Sensing of Environment*, 240, 111685.
- Claverie, M., Ju, J., Masek, J.G., Dungan, J.L., Vermote, E.F., Roger, J.C., Skakun, S.V., & Justice, C. (2018). The harmonized landsat and sentinel-2 surface reflectance data set. *Remote Sensing of Environment*, 219, 145 – 161.
- Elmore, A.J., Guinn, S.M., Minsley, B.J., & Richardson, A.D. (2012). Landscape controls on the timing of spring, autumn, and growing season length in mid-Atlantic forests. *Global Change Biology*, 18, 656–674. doi:10.1111/j.1365-2486.2011.02521.x.
- Ferrari, S., & Cribari-Neto, F. (2004). Beta regression for modelling rates and proportions. *Journal of Applied Statistics*, 31, 799–815.
- Finley, A.O., & Babcock, C. (2020). rsBayes: Bayesian inference for remotely sensed phenomena. URL: <https://github.com/finleya/rsBayes>. r package version 0.1.0.
- Fisher, J.I., Mustard, J.F., & Vadeboncoeur, M.A. (2006). Green leaf phenology at landsat resolution: Scaling from the field to the satellite. *Remote Sensing of Environment*, 100, 265 – 279.
- Ganguly, S., Friedl, M.A., Tan, B., Zhang, X., & Verma, M. (2010). Land surface phenology from modis: Characterization of the collection 5 global land cover dynamics product. *Remote Sensing of Environment*, 114, 1805 – 1816.
- Gelman, A., Carlin, J., Stern, H., Dunson, D., Vehtari, A., & Rubin, D. (2013). *Bayesian Data Analysis*, Third Edition. Chapman & Hall/CRC Texts in Statistical Science, Taylor & Francis.
- Goward, S.N., Tucker, C.J., & Dye, D.G. (1985). North American vegetation patterns observed with the NOAA-7 advanced very high resolution radiometer. *Vegetatio*, 64.
- Greene, W.H. (2008). *Econometric Analysis*. 8 ed., Pearson, New York, NY.
- Hegde, L.M., & Dahiya, R.C. (1989). Estimation of the parameters in a truncated normal distribution. *Communications in Statistics - Theory and Methods*, 18, 4177–4195.
- Henderson, K., & Badhwar, G. (1984). An initial model for estimating soybean development stages from spectral data. *Remote Sensing of Environment*, 14, 55–63.
- Jeong, S.J., Ho, C.H., Gim, H.J., & Brown, M.E. (2011). Phenology shifts at start vs. end of growing season in temperate vegetation over the northern hemisphere for the period 1982–2008. *Global Change Biology*, 17, 2385–2399.
- Kowalski, K., Senf, C., Hostert, P., & Pflugmacher, D. (2020). Characterizing spring phenology of temperate broadleaf forests using landsat and sentinel-2 time series. *International Journal of Applied Earth Observation and Geoinformation*, 92, 102172.
- Li, J., & Roy, D. (2017). A Global Analysis of Sentinel-2A, Sentinel-2B and Landsat-8 Data Revisit Intervals and Implications for Terrestrial Monitoring. *Remote Sensing*, 9, 902.
- Melaas, E.K., Friedl, M.A., & Zhu, Z. (2013). Detecting interannual variation in deciduous broadleaf forest phenology using Landsat TM/ETM+ data. *Remote Sensing of Environment*, 132, 176–185.
- Morisette, J.T., Richardson, A.D., Knapp, A.K., Fisher, J.I., Graham, E.A., Abatzoglou, J., Wilson, B.E., Breshears, D.D., Henebry, G.M., Hanes, J.M., & Liang, L. (2009). Tracking the rhythm of the seasons in the face of global change: phenological research in the 21st century. *Frontiers in Ecology and the Environment*, 7, 253–260.
- Parmesan, C., & Yohe, G. (2003). A globally coherent fingerprint of climate change impacts across natural systems. *Nature*, 421, 37–42.
- Piao, S., Liu, Q., Chen, A., Janssens, I.A., Fu, Y., Dai, J., Liu, L., Lian, X., Shen, M., & Zhu, X. (2019). Plant phenology and global climate change: Current progresses and challenges. *Global Change Biology*, 25, 1922–1940.
- Rea, J., & Ashley, M. (1976). Phenological evaluations using Landsat-1 sensors. *International Journal of Biometeorology*, 20, 240–248.
- Senf, C., Pflugmacher, D., Heurich, M., & Krueger, T. (2017). A Bayesian hierarchical model for estimating spatial and temporal variation in vegetation phenology from Landsat time series. *Remote Sensing of Environment*, 194, 155–160.
- Smithson, M., & Verkuilen, J. (2006). A better lemon squeezer? maximum-likelihood regression with beta-distributed dependent variables. *Psychological methods*, 11, 54–71.
- Spanner, M.A., Pierce, L.L., Running, S.W., & Peterson, D.L. (1990). The seasonality of avhrr data of temperate coniferous forests: Relationship with leaf area index. *Remote Sensing of Environment*, 33, 97–112.
- Sulla-Menashe, D., Gray, J.M., Abercrombie, S.P., & Friedl, M.A. (2019). Hierarchical mapping of annual global land cover 2001 to present: The MODIS Collection 6 Land Cover product. *Remote Sensing of Environment*, 222, 183–194.
- Taylor, B., Dini, P., & Kidson, J. (1985). Determination of seasonal and interannual variation in New Zealand pasture growth from NOAA-7 data. *Remote Sensing of Environment*, 18, 177–192.
- USGS (2020). National Agriculture Imagery Program (NAIP). URL: <https://www.usgs.gov/centers/eros>.
- Vorobiova, N., & Chernov, A. (2017). Curve fitting of modis ndvi time series in the task of early crops identification by satellite images. *Procedia Engineering*, 201, 184–195. 3rd International Conference Information Technology and Nanotechnology.
- Yang, L., Jin, S., Danielson, P., Homer, C., Gass, L., Bender, S.M., Case, A., Costello, C., Dewitz, J., Fry, J., Funk, M., Granneman, B., Liknes, G.C., Rigge, M., & Xian, G. (2018). A new generation of the united states national land cover

- database: Requirements, research priorities, design, and implementation strategies. *ISPRS Journal of Photogrammetry and Remote Sensing*, 146, 108 – 123.
- Zeng, L., Wardlow, B.D., Xiang, D., Hu, S., & Li, D. (2020). A review of vegetation phenological metrics extraction using time-series, multispectral satellite data. *Remote Sensing of Environment*, 237, 111511.
- Zhang, X., Friedl, M.A., Schaaf, C.B., Strahler, A.H., Hodges, J.C., Gao, F., Reed, B.C., & Huete, A. (2003). Monitoring vegetation phenology using modis. *Remote Sensing of Environment*, 84, 471 – 475.
- Zhang, X., Liu, L., Liu, Y., Jayavelu, S., Wang, J., Moon, M., Henebry, G.M., Friedl, M.A., & Schaaf, C.B. (2018). Generation and evaluation of the VIIRS land surface phenology product. *Remote Sensing of Environment*, 216, 212 – 229.

Supplementary material

4.1. Supplementary figures

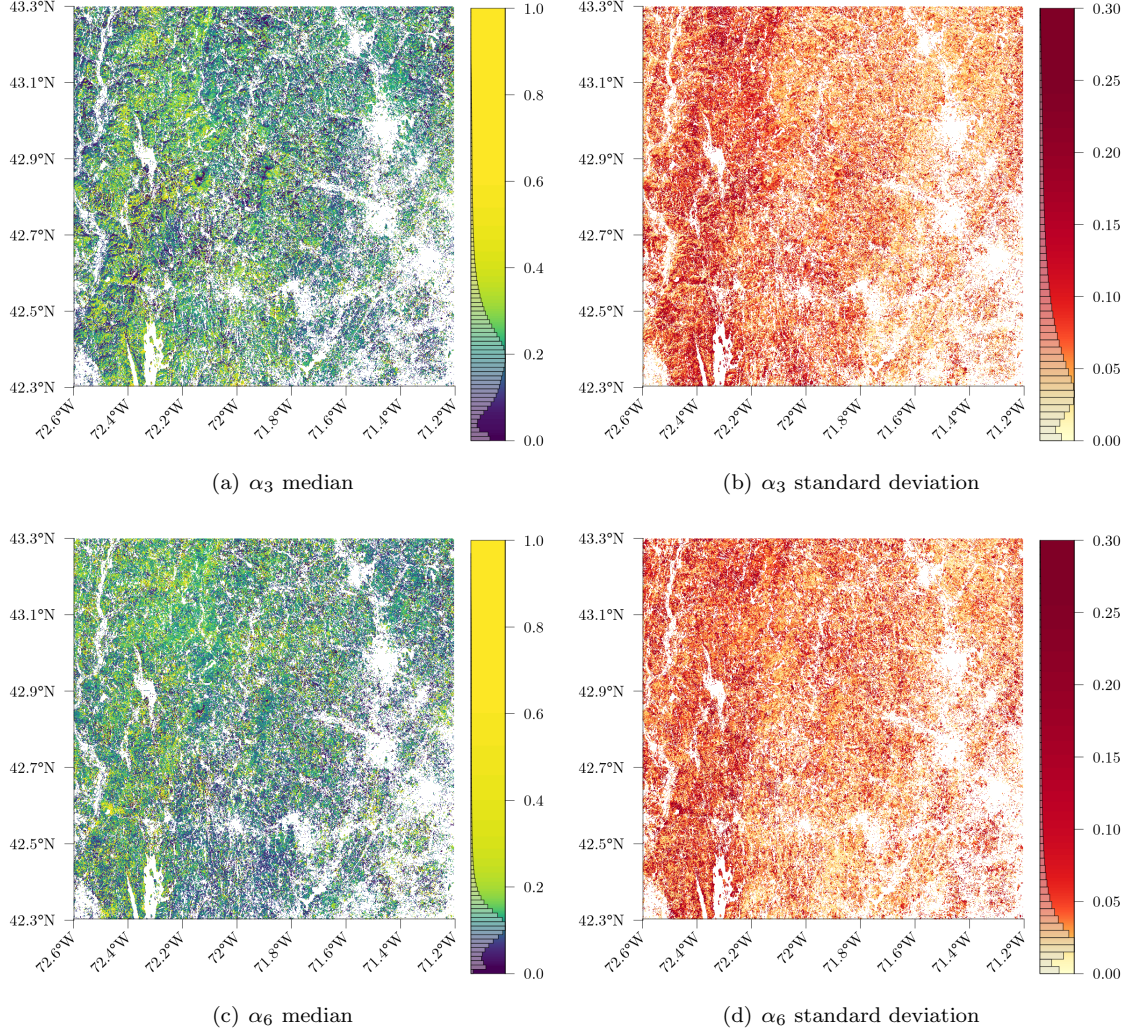


Figure S1: Maps showing spatial distribution of long-term average (2013-2019) α_3 and α_6 point and uncertainty estimates using the Bayesian LSP model.

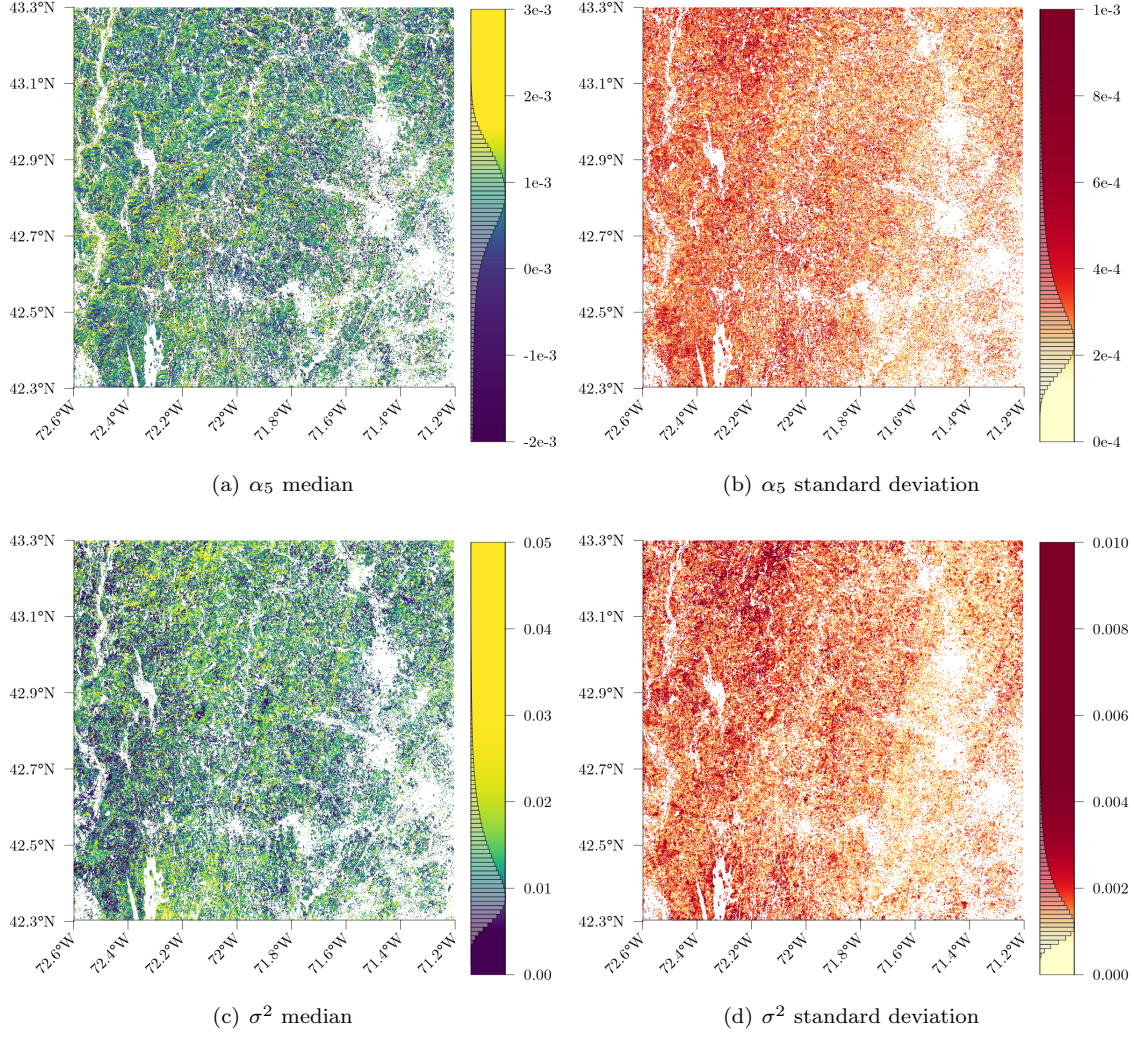


Figure S2: Maps showing spatial distribution of long-term average (2013-2019) α_2 and α_5 point and uncertainty estimates using the Bayesian LSP model.

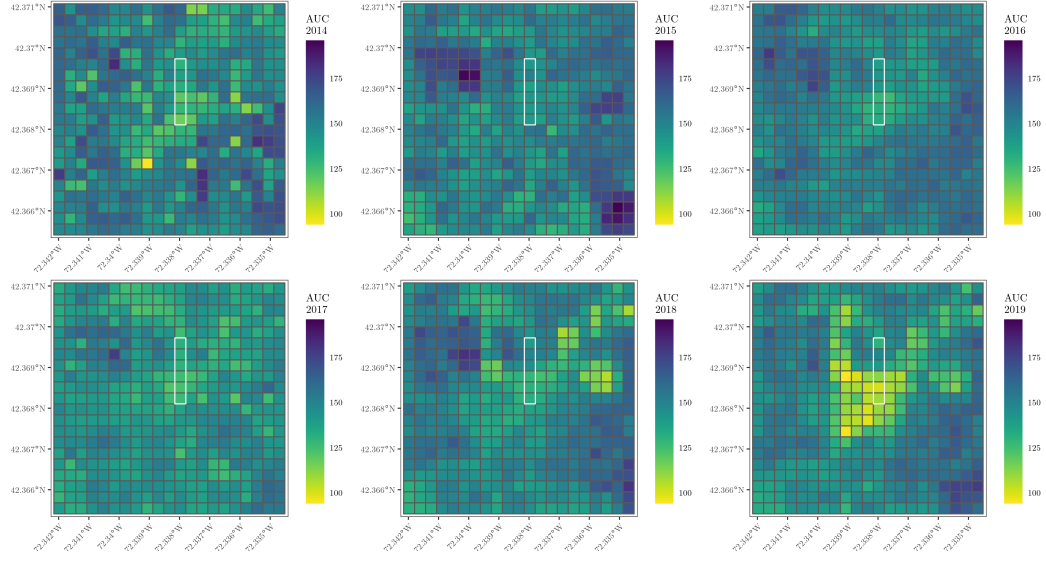


Figure S3: Supplement to Figure 9 that provides pixel-level area under the curve (AUC) posterior distribution median estimates for all years in the study period.

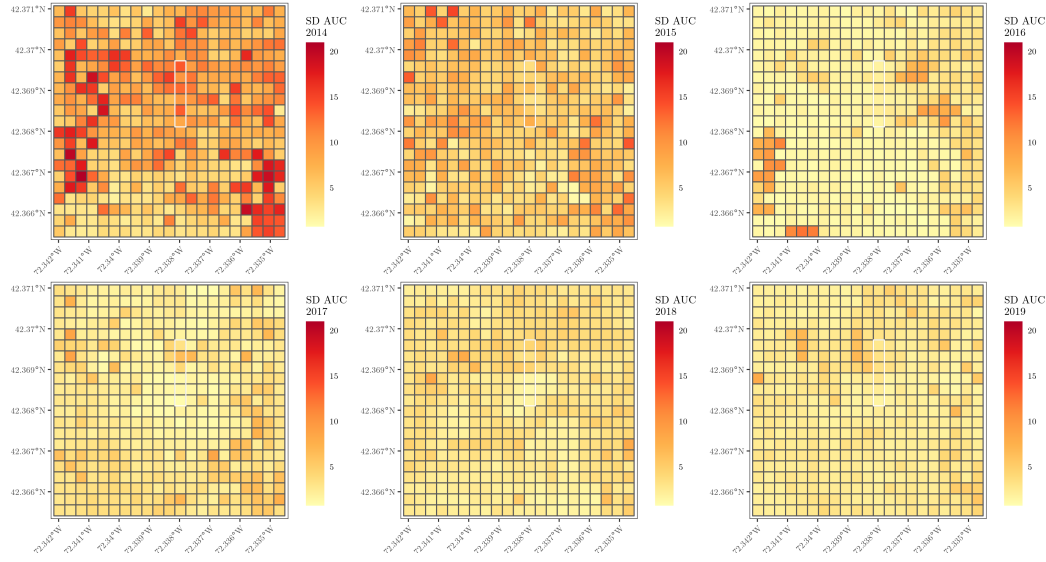


Figure S4: Supplement to Figures 9 and S3 that provides pixel-level area under the curve (AUC) posterior distribution standard deviation (SD) estimates for all years in the study period.

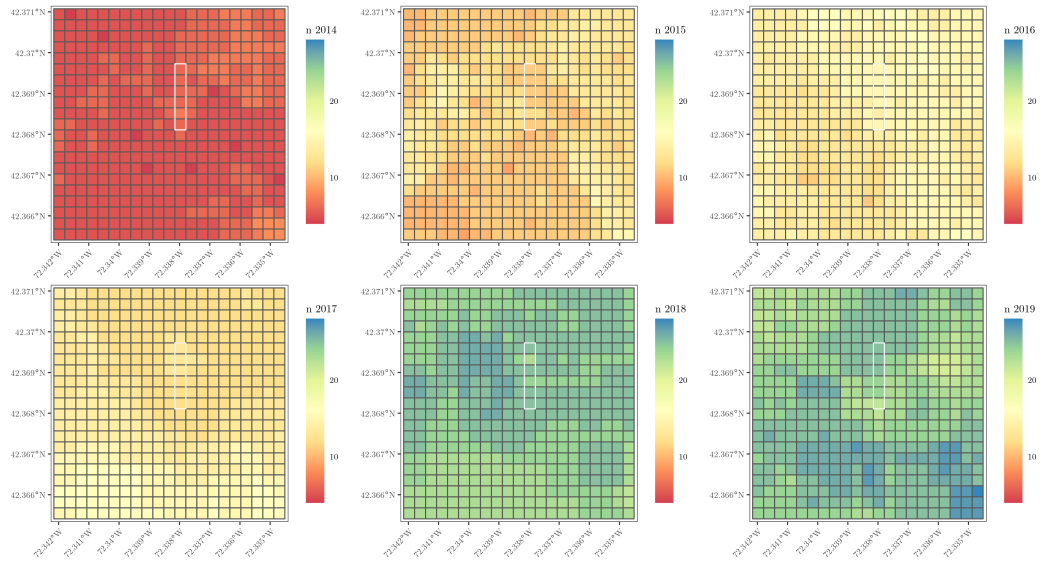


Figure S5: Supplement to Figures 9, S3, and S3 that provides pixel-level sample size (n) used to estimate area under the curve (AUC) posterior distribution all years in the study period.

4.2. Reproduce portions of manuscript Section 3.3 using `pheno`

The R code below reproduces key portions of the analysis in manuscript Section 3.3. We begin by loading the necessary packages and scripts. The current version of **rsBayes** 0.1.1 is required and can be obtained from its git repository using the code below.

```
R> library(devtools)
R> devtools::install_github("finleya/rsBayes")
```

```
R> library(rsBayes)
R>
R> ##for plotting
R> library(sp)
R> library(sf)
R> library(dplyr)
R> library(ggplot2)
R> library(cowplot)
R> library(viridis)
```

The HLS EVI data used in manuscript Section 3.3 is available in the R **rsBayes** package's `aoi_hls` dataset.

```
R> head(aoi_hls)

## # A tibble: 6 x 7
##   pixel      x      y sat   year  doy  evi
##   <dbl> <dbl> <dbl> <fct> <int> <int> <dbl>
## 1     1 718875 4694385 L30   2014    4   NA
## 2     1 718875 4694385 L30   2014   13   NA
## 3     1 718875 4694385 L30   2014   20   NA
## 4     1 718875 4694385 L30   2014   29   NA
## 5     1 718875 4694385 L30   2014   36   NA
## 6     1 718875 4694385 L30   2014   45   NA
```

The **rsBayes** package `pheno` function implements all methods in manuscript Section 2. The code below generates MCMC samples for model parameters for each pixel of 2019 EVI data.

```
R> pixels.2019 <- aoi_hls %>% filter(year == 2019)
R>
R> n.pixels <- length(unique(pixels.2019$pixel))
R>
R> pixel.list <- list() ##save each pixel's pheno model output
R>
R> set.seed(1)
R>
R> for(i in 1:n.pixels){
+   pixel.dat <- subset(pixels.2019, pixel == i) ##get data for the i-th pixel
+   pixel.list[[i]] <- pheno(evi~doy, data=pixel.dat, family="beta",
+                           starting=list(alpha.1=0.2, alpha.2=0.5, alpha.3=0.25,
+                                         alpha.4=100, alpha.5=0.0001, alpha.6=0.25,
```

```

+             alpha.7=200, sigma.sq=0.001),
+             tuning=list(alpha.1=0.001, alpha.2=0.01, alpha.3=0.01,
+             alpha.4=0.5, alpha.5=0.0001, alpha.6=0.01,
+             alpha.7=1, sigma.sq=0.1),
+             priors=list(alpha=list(alpha.5=c(-0.001, 0.001)),
+             sigma.sq.IG=c(2, 0.001)),
+             n.samples=50000,
+             sub.sample=list("start"=25000, thin=25), verbose = FALSE)
+ }

```

Note, each object in the `pixel.list` is a `pheno` model class that holds the respective pixel model information and MCMC samples. The code below checks the class then prints parameter estimates for the first pixel.

```

R> class(pixel.list[[1]])

## [1] "pheno"

R> summary(pixel.list[[1]])

## Chain sub.sample:
## start = 1
## end = 1001
## thin = 1
## samples size = 1001
##      2.5%    25%    50%    75%    97.5%
## alpha.1 0.1788 0.1969 0.2081 0.2160 0.2262
## alpha.2 0.4914 0.5656 0.5948 0.6155 0.6490
## alpha.3 0.0715 0.0965 0.1131 0.1365 0.1771
## alpha.4 133.8739 136.5704 137.6818 138.6741 140.8830
## alpha.5 0.0004 0.0007 0.0009 0.0009 0.0010
## alpha.6 0.0712 0.0940 0.1060 0.1228 0.1699
## alpha.7 286.5546 290.2408 292.1101 294.1779 298.4399
## sigma.sq 0.0020 0.0028 0.0034 0.0041 0.0067

```

Now using the post convergence MCMC samples compute posterior samples for the area under the curve (AUC) then generate several summary statistics for the AUC posterior.

```

R> G <- function(t, alpha){
+   ifelse(t <= (alpha[3]*alpha[4]+alpha[6]*alpha[7])/(alpha[3]+alpha[6]),
+   alpha[1] + (alpha[2] - alpha[5]*t)/(1.0 + exp(-alpha[3]*(t-alpha[4]))),
+   alpha[1] + (alpha[2] - alpha[5]*t)/(1.0 + exp(-alpha[6]*(alpha[7]-t)))
+   )
+ }
R>
R> my.summary <- function(x){
+   q <- quantile(x, probs=c(0.5, 0.05, 0.975))
+   c(mean(x), sd(x), q[1], q[3]-q[2])
+ }
R>
R> post.auc <- t(as.data.frame(lapply(pixel.list, function(x){

```

```

+   my.summary(apply(x$p.theta.samples, 1, function(v){
+     integrate(G, lower = 1, upper = 365, v)[1]$value)})))))
R>
R> rownames(post.auc) <- NULL
R> colnames(post.auc) <- c("auc.mean", "auc.sd", "auc.median", "auc.q95.width")

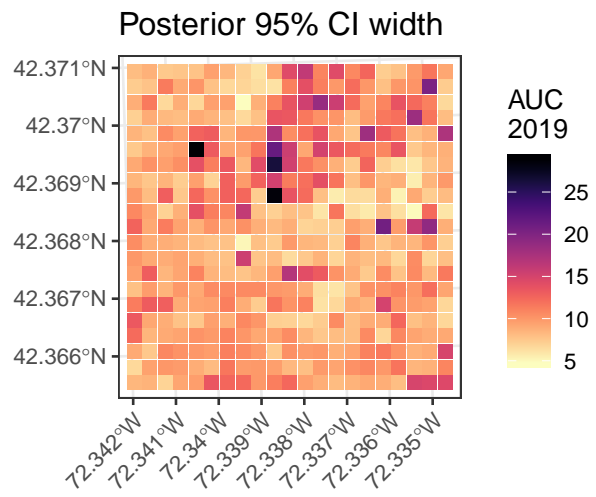
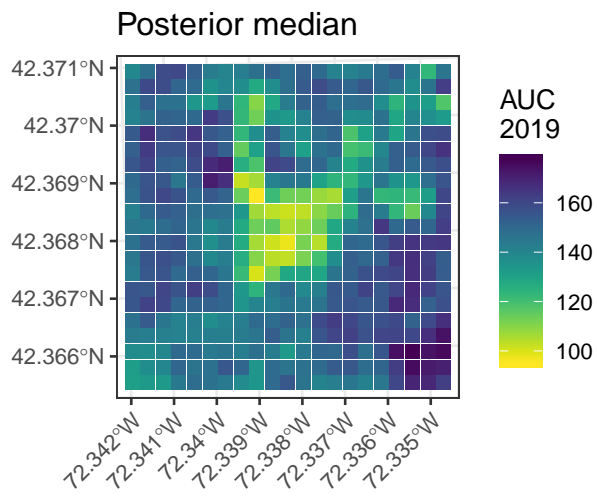
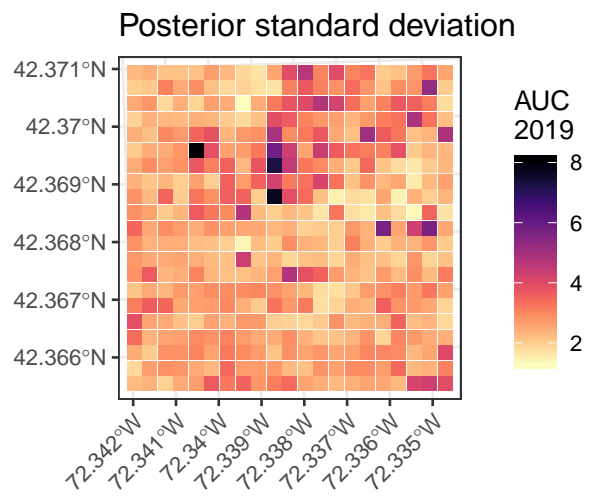
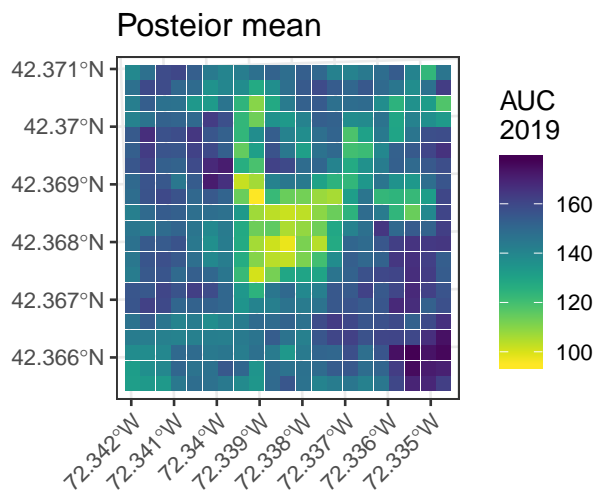
```

The next bit of code joins the pixel coordinates with their respective posterior summaries, converts them to spatial objects, then plots a few of the summaries. Note the plot labeled “Posterior median” is the same as manuscript Figure 9(f). The other figures are provided to illustrate how other summary statistics are generated and mapped for the given posterior.

```

R> ##get the coordinates for each pixel
R> df <- pixels.2019 %>% group_by(pixel) %>% slice(1) %>% select(pixel, x, y)
R>
R> #join with posterior summaries and create spatial object
R> df <- cbind(as.data.frame(df), post.auc)
R>
R> coordinates(df) <- c("x", "y")
R> proj4string(df) <- "+proj=utm +zone=18 +ellps=WGS84 +units=m +no_defs"
R> sf.df <- as(df, "sf")
R>
R> ##make plots
R> size <- 2.5
R> auc.mean <- ggplot(sf.df) +
+   geom_sf(data = sf.df, aes(color = auc.mean), size=size, shape=15) +
+   scale_color_viridis("AUC\n2019", direction = -1) +
+   ggtitle("Posterior mean") +
+   theme_bw() + theme(axis.text.x = element_text(angle = 45, hjust = 1))
R>
R> auc.sd <- ggplot(sf.df) +
+   geom_sf(data = sf.df, aes(color = auc.sd), size=size, shape=15) +
+   scale_color_viridis("AUC\n2019", option="A", direction = -1) +
+   ggtitle("Posterior standard deviation") +
+   theme_bw() + theme(axis.text.x = element_text(angle = 45, hjust = 1))
R>
R> auc.median <- ggplot(sf.df) +
+   geom_sf(data = sf.df, aes(color = auc.median), size=size, shape=15) +
+   scale_color_viridis("AUC\n2019", direction = -1) +
+   ggtitle("Posterior median") +
+   theme_bw() + theme(axis.text.x = element_text(angle = 45, hjust = 1))
R>
R> auc.q95.width <- ggplot(sf.df) +
+   geom_sf(data = sf.df, aes(color = auc.q95.width), size=size, shape=15) +
+   scale_color_viridis("AUC\n2019", option="A", direction = -1) +
+   ggtitle("Posterior 95% CI width") +
+   theme_bw() + theme(axis.text.x = element_text(angle = 45, hjust = 1))
R>
R> plot_grid(auc.mean, auc.sd, auc.median, auc.q95.width, align="hv")

```



4.3. Run `phenoBrick` for `RasterBrick` object using multiple CPU cores

The R code below uses the `phenoBrick` function to fit the Bayesian LSP model presented in manuscript Section 2. The R code that defines the `phenoBrick` function is given in Section 4.4 of this supplement. R-like documentation for `phenoBrick` is provided in Section 4.5 of this supplement. We use the AOI for manuscript Section 3.3 as our example dataset—this time formatted as a `RasterBrick` object.

The following code chunk loads the necessary packages and the `phenoBrick` function. Note that the code defining the `phenoBrick` function is suppressed in this portion of the supplement to make the code in this document easier to follow.

```
R> library(rsBayes)
R>
R> ## needed for phenoBrick function
R> library(raster)
R> library(doSNOW)
R> library(progress)
R>
R> ## needed for plotting
R> library(sf)
R> library(ggplot2)
R> library(cowplot)
R> library(viridis)
R>
R> ## phenoBrick function code suppressed for Supplementary Material pdf
```

The next piece of code loads the `aoi_hls_rast` and `aoi_hls_rast_info` data objects. The `aoi_hls_rast` object holds the same VI data as `rsBayes::aoi_hls` only in a `RasterBrick` format. The `aoi_hls_rast_info` object holds the DOY metadata for each of the 651 bands in `aoi_hls_rast`. Row one of `aoi_hls_rast_info` corresponds to band 1 of `aoi_hls_rast` and so on.

```
R> class(aoi_hls_rast)

## [1] "RasterBrick"
## attr(,"package")
## [1] "raster"

R> nlayers(aoi_hls_rast)

## [1] 651

R> head(aoi_hls_rast_info)

##   sat year doy
## 1 L30 2013 106
## 2 L30 2013 113
## 3 L30 2013 122
## 4 L30 2013 138
## 5 L30 2013 145
## 6 L30 2013 154

R> dim(aoi_hls_rast_info)

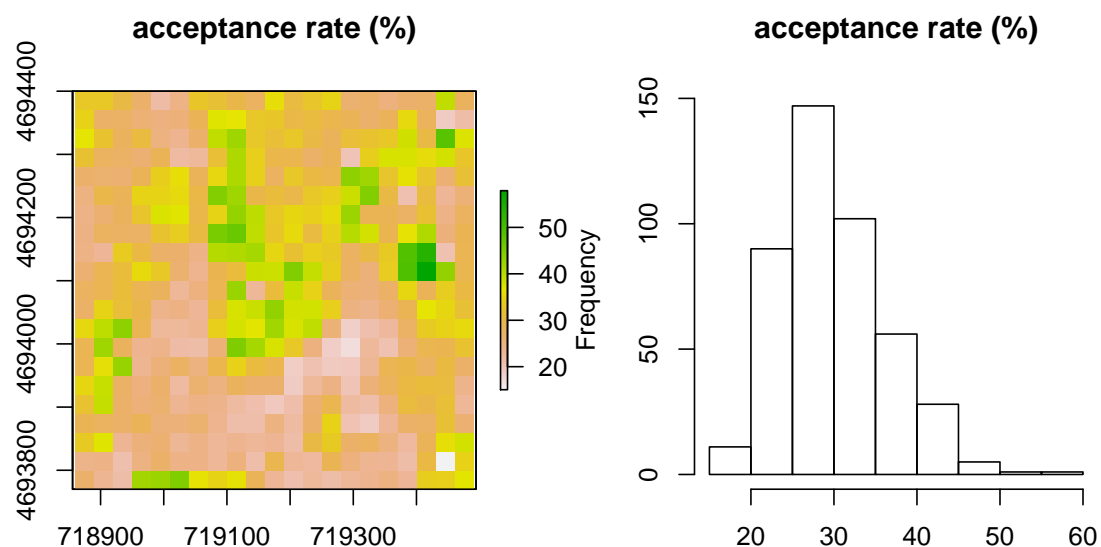
## [1] 651   3
```

The following code sets the necessary starting, tuning, and prior values for **phenoBrick** in the same list format used for **pheno**. The code below also sets the number of MCMC samples and subsets the resulting MCMC samples for subsequent summarization. The number of CPU cores for **phenoBrick** to use is also set here.

```
R> ## set starting values
R> starting <- list(alpha.1=0.2, alpha.2=0.5, alpha.3=0.25, alpha.4=100, alpha.5=0.0001,
+                 alpha.6=0.25, alpha.7=200, sigma.sq=0.001)
R> ## set tuning values
R> tuning <- list(alpha.1=0.001, alpha.2=0.001, alpha.3=0.005, alpha.4=0.5, alpha.5=0.0001,
+               alpha.6=0.005, alpha.7=0.5, sigma.sq=0.03)
R> ## set priors
R> priors <- list(alpha=list(alpha.5=c(-0.001, 0.001)), sigma.sq.IG=c(2, 0.001))
R> ## set number of MCMC samples
R> n.samples <- 50000
R> sub.sample <- list("start" = 25001, "thin" = 25)
R> ## set the number of CPU cores phenoBrick should use
R> n.cores <- 2
R> set.seed(1)
R> modBrick <- phenoBrick(VI.rast = aoi_hls_rast, doy = aoi_hls_rast_info$doy, family = "beta",
+                       starting = starting, tuning = tuning, priors = priors,
+                       n.samples = n.samples, sub.sample = sub.sample, n.cores = n.cores)
```

The **modBrick** object is a list of 9 **RasterBrick** objects. The first 8 hold the subsetting MCMC samples for the α and σ^2 parameters—1 for each parameter. The Metropolis acceptance rates for each pixel are held in **modBrick\$acc.rate**. The following figure maps the acceptance rate (left) and shows a histogram of the pixel acceptance rates (right). It is evident that only a few pixels fall outside the 20-50 percent range.

```
R> par(mfrow = c(1,2))
R> plot(modBrick$acc.rate[[1]], main = "acceptance rate (%)")
R> hist(modBrick$acc.rate[[1]], main = "acceptance rate (%)", xlab = "")
```



The next piece of code calculates posterior medians and standard deviations for α_1 and for season length ($\alpha_7 - \alpha_4$).

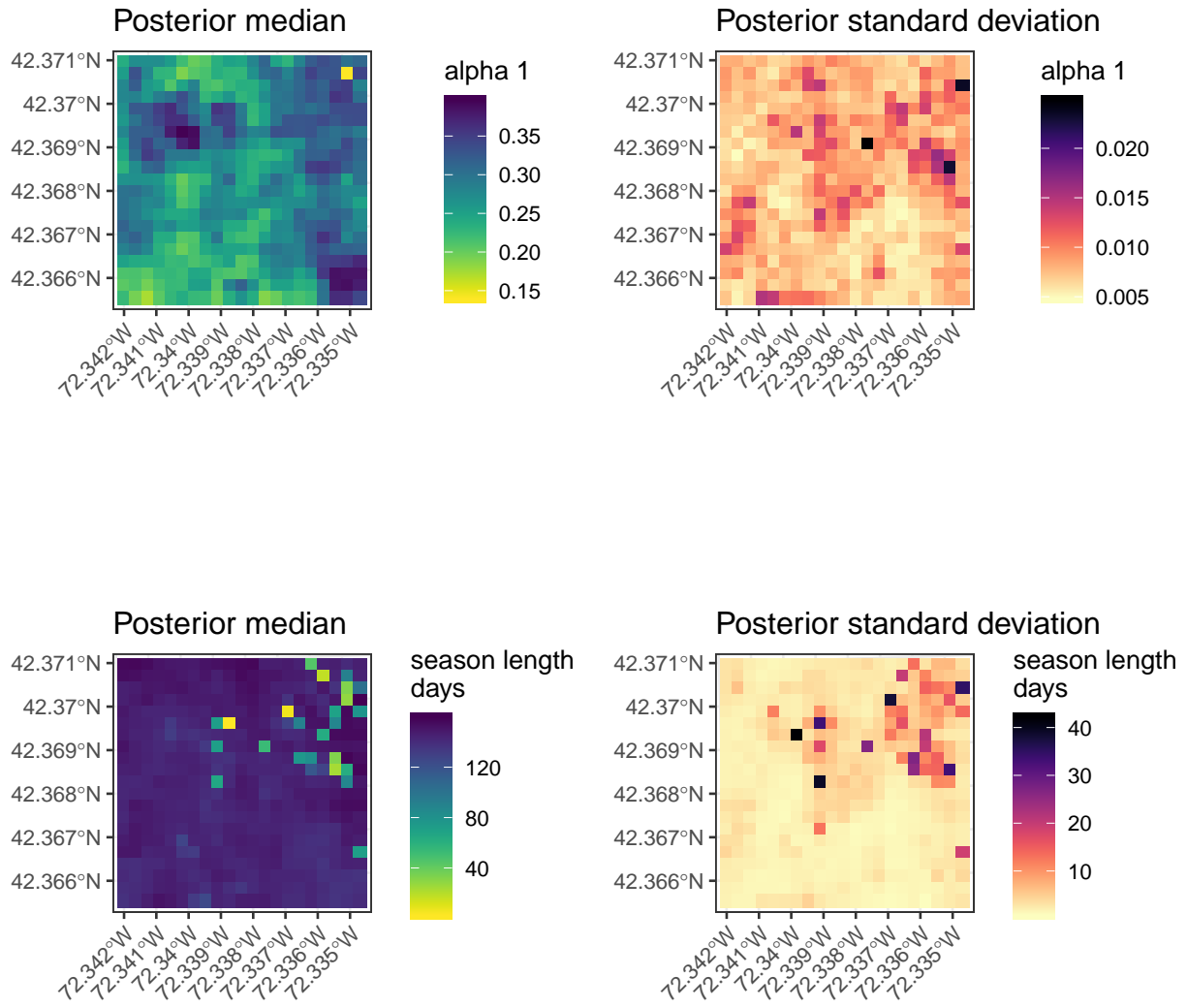
```
R> ## calculate posterior medians for alpha.1
R> alpha1.median <- stackApply(modBrick$alpha1.samps,1,median)
R>
R> ## calculate posterior standard deviations for alpha.1
R> alpha1.sd <- stackApply(modBrick$alpha1.samps,1,sd)
R>
R> ## calculate posterior medians for season length (alpha.7 - alpha.4)
R> season.length.median <-stackApply(modBrick$alpha7.samps-modBrick$alpha4.samps,1,median)
R>
R> ## calculate posterior standard deviations for season length (alpha.7 - alpha.4)
R> season.length.sd <- stackApply(modBrick$alpha7.samps-modBrick$alpha4.samps,1,sd)
```

The following converts the summary `RasterLayer` objects to `sf` objects for plotting purposes.

```
R> ## convert to sf for ggplot
R> alpha1.median <- as(as(alpha1.median, "SpatialPixelsDataFrame"),"sf")
R> names(alpha1.median)[1] <- "alpha1.median"
R>
R> alpha1.sd <- as(as(alpha1.sd, "SpatialPixelsDataFrame"),"sf")
R> names(alpha1.sd)[1] <- "alpha1.sd"
R>
R> season.length.median <- as(as(season.length.median, "SpatialPixelsDataFrame"),"sf")
R> names(season.length.median)[1] <- "season.length.median"
R>
R> season.length.sd <- as(as(season.length.sd, "SpatialPixelsDataFrame"),"sf")
R> names(season.length.sd)[1] <- "season.length.sd"
```

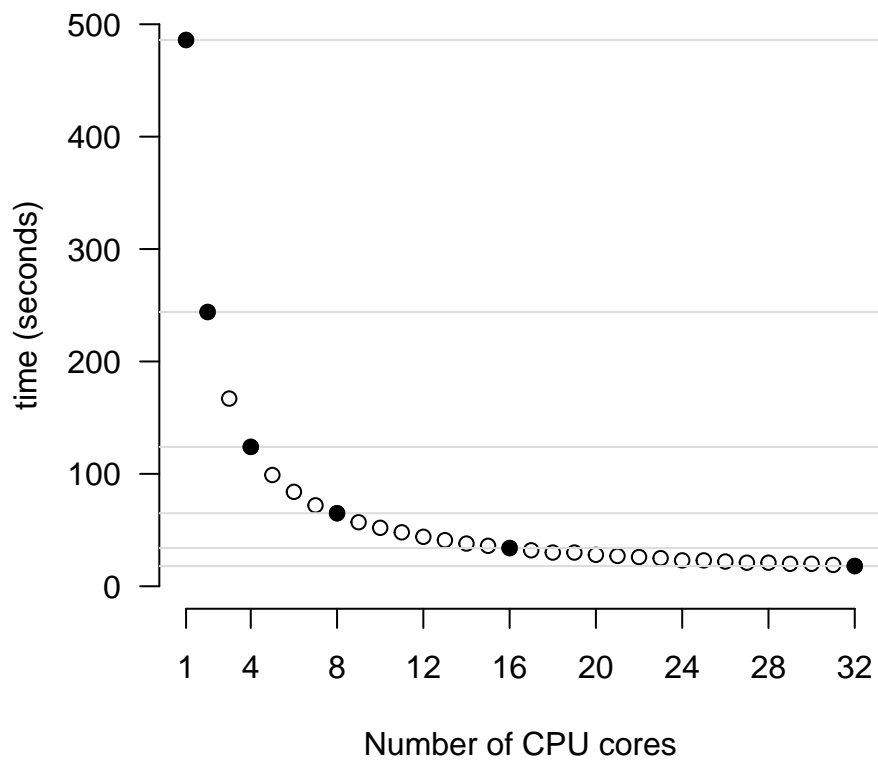
The next code chunk generates maps of the posterior medians and standard deviations for α_1 and season length ($\alpha_7 - \alpha_4$).

```
R> ## make maps
R> size <- 2.5
R>
R> alpha1.median.plt <- ggplot(alpha1.median) +
+   geom_sf(data = alpha1.median, aes(color = alpha1.median),
+         size=size, shape=15) +
+   scale_color_viridis("alpha 1", direction = -1) +
+   ggtitle("Posterior median") +
+   theme_bw() + theme(axis.text.x = element_text(angle = 45, hjust = 1))
R>
R> alpha1.sd.plt <- ggplot(alpha1.sd) +
+   geom_sf(data = alpha1.sd, aes(color = alpha1.sd),
+         size=size, shape=15) +
+   scale_color_viridis("alpha 1", option="A", direction = -1) +
+   ggtitle("Posterior standard deviation") +
+   theme_bw() + theme(axis.text.x = element_text(angle = 45, hjust = 1))
R>
R> season.length.median.plt <- ggplot(season.length.median) +
+   geom_sf(data = season.length.median, aes(color = season.length.median),
+         size=size, shape=15) +
+   scale_color_viridis("season length\ndays", direction = -1) +
+   ggtitle("Posterior median") +
+   theme_bw() + theme(axis.text.x = element_text(angle = 45, hjust = 1))
R>
R> season.length.sd.plt <- ggplot(season.length.sd) +
+   geom_sf(data = season.length.sd, aes(color = season.length.sd),
+         size=size, shape=15) +
+   scale_color_viridis("season length\ndays", option="A", direction = -1) +
+   ggtitle("Posterior standard deviation") +
+   theme_bw() + theme(axis.text.x = element_text(angle = 45, hjust = 1))
R>
R> plot_grid(alpha1.median.plt, alpha1.sd.plt,
+   season.length.median.plt, season.length.sd.plt, align = "hv")
```



Results of a time test of **phenoBrick** are shown in the following figure. This test was carried out on a Linux workstation with 128 GBs of RAM and an AMD 3970X 32 core processor. The filled in points are at 1, 2, 4, 8, 16, and 32 cores. It is evident from the figure that the run time is halved when the number of cores used is doubled.

```
R> time.test <- cbind(1:32,c(486,244,167,124,99,84,72,65,57,52,48,44,41,38,36,34,32,30,
+                           30,28,27,26,25,23,23,22,21,21,20,20,19,18))
R>
R> plot(time.test, bty = "n", ylab = "time (seconds)", xlab = "Number of CPU cores",
+       axes = F, ylim = c(0,500))
R> axis(1, at = c(1,4,8,12,16,20,24,28,32))
R> axis(2, at = c(0,100,200,300,400,500), las = 2)
R> abline(h = time.test[c(1,2,4,8,16,32),2], col = "gainsboro")
R> points(time.test[c(1,2,4,8,16,32),], pch = 19)
```



4.4. R code to create the phenoBrick function

```
R> phenoBrick

## function(VI.rast, doy, gamma = c(0, 1), family = "normal", starting, tuning, priors, n.samples, sub.sample, n.cores = 1,
##          eval.rast, t.normal.bounds = c(0,1)){
##
##   if(missing(sub.sample)){sub.sample <- list("start" = 1, "thin" = 1, "end" = n.samples)}
##
##   if(!("end" %in% names(sub.sample))){sub.sample$end <- n.samples}
##
##   n.samples.keep <- length(seq(as.integer(sub.sample$start), as.integer(sub.sample$end), by=as.integer(sub.sample$thin)))
##
##   rast.dim <- dim(VI.rast)
##
##   cl <- makeCluster(n.cores)
##   registerDoSNOW(cl)
##
##   alpha1.samps <- brick(extent(VI.rast),nrows=rast.dim[1],ncols=rast.dim[2],nl=n.samples.keep,crs=proj4string(VI.rast))
##   alpha2.samps <- brick(extent(VI.rast),nrows=rast.dim[1],ncols=rast.dim[2],nl=n.samples.keep,crs=proj4string(VI.rast))
##   alpha3.samps <- brick(extent(VI.rast),nrows=rast.dim[1],ncols=rast.dim[2],nl=n.samples.keep,crs=proj4string(VI.rast))
##   alpha4.samps <- brick(extent(VI.rast),nrows=rast.dim[1],ncols=rast.dim[2],nl=n.samples.keep,crs=proj4string(VI.rast))
##   alpha5.samps <- brick(extent(VI.rast),nrows=rast.dim[1],ncols=rast.dim[2],nl=n.samples.keep,crs=proj4string(VI.rast))
##   alpha6.samps <- brick(extent(VI.rast),nrows=rast.dim[1],ncols=rast.dim[2],nl=n.samples.keep,crs=proj4string(VI.rast))
##   alpha7.samps <- brick(extent(VI.rast),nrows=rast.dim[1],ncols=rast.dim[2],nl=n.samples.keep,crs=proj4string(VI.rast))
##   sigma2.samps <- brick(extent(VI.rast),nrows=rast.dim[1],ncols=rast.dim[2],nl=n.samples.keep,crs=proj4string(VI.rast))
##   acc.rate <- brick(extent(VI.rast),nrows=rast.dim[1],ncols=rast.dim[2],nl=2,crs=proj4string(VI.rast))
##
##   run.idx <- 1:(rast.dim[1]*rast.dim[2])
##   if(!missing(eval.rast)){run.idx <- run.idx[eval.rast[,1]]}
##
##   pb <- progress_bar$new(format = "[:bar] :percent | elapsed: :elapsedfull", total = length(run.idx), clear = FALSE)
##   progress <- function(n){pb$tick()}
##   opts <- list(progress = progress)
##
##   res <-
##     foreach(i=1:length(run.idx),.packages = c("raster","coda","rsBayes"),.combine="rbind",.options.snow=opts)%dopar%{
##
##     idx <- run.idx[i]
##     y <- as.vector(VI.rast[idx])
##     t <- doy[!is.na(y)]
##     y <- y[!is.na(y)]
##
##     out <- pheno(y ~ t, priors=priors, n.samples=n.samples, sub.sample = sub.sample, starting = starting,
##                 tuning=tuning, family=family, verbose = F, t.normal.bounds = t.normal.bounds, gamma = gamma)
##
##     rbind(t(out$p.theta.samples),out$MH.acceptance)
##
##   }
##   stopCluster(cl)
##   nrow.res <- nrow(res)
##
##   alpha1.samps[run.idx] <- res[seq(1,nrow.res,9),]
##   alpha2.samps[run.idx] <- res[seq(2,nrow.res,9),]
##   alpha3.samps[run.idx] <- res[seq(3,nrow.res,9),]
##   alpha4.samps[run.idx] <- res[seq(4,nrow.res,9),]
##   alpha5.samps[run.idx] <- res[seq(5,nrow.res,9),]
##   alpha6.samps[run.idx] <- res[seq(6,nrow.res,9),]
##   alpha7.samps[run.idx] <- res[seq(7,nrow.res,9),]
##   sigma2.samps[run.idx] <- res[seq(8,nrow.res,9),]
##   acc.rate[run.idx] <- res[seq(9,nrow.res,9),1:2]
##
##   return(list("alpha1.samps" = alpha1.samps, "alpha2.samps" = alpha2.samps, "alpha3.samps" = alpha3.samps,
##              "alpha4.samps" = alpha4.samps, "alpha5.samps" = alpha5.samps, "alpha6.samps" = alpha6.samps,
##              "alpha7.samps" = alpha7.samps, "sigma2.samps" = sigma2.samps, "acc.rate" = acc.rate))
## }
```

4.5. Documentation for `phenoBrick`

<code>phenoBrick</code>	<i>phenoBrick</i>
<i>Description</i>	
Function to run <code>rsBayes::pheno</code> for a vegetation index (VI) time series raster using multiple CPU cores.	
<i>Usage</i>	
<pre>phenoBrick(VI.rast, doy, gamma = c(0, 1), family = "normal", starting, tuning, priors, n.samples, sub.sample, n.cores = 1, eval.rast, t.normal.bounds = c(0,1))</pre>	
<i>Arguments</i>	
<code>VI.rast</code>	a <code>RasterBrick</code> object holding the observed VIs. Each band holds VI observations for a specific day of the year (DOY). There should be as many bands as there are observation DOYs. NAs can be included where VI observations are missing.
<code>doy</code>	a numeric vector of length <code>nlayers(VI.rast)</code> holding DOYs that correspond to the DOYs for each band in <code>VI.rast</code> .
<code>gamma</code>	a vector of length two that holds the VI variable's theoretical bounds. Lower and upper bounds are given in element 1 and 2, respectively. These must be finite values.
<code>family</code>	a quoted string that indicates which likelihood to use for modeling the VI variable. Options are Beta, Normal, and truncated Normal, specified using quoted argument values <code>beta</code> , <code>normal</code> , and <code>t.normal</code> , respectively. The σ^2 parameter is the variance for the Beta, Normal, and truncated Normal likelihoods. See Details for VI variable's support for each likelihood.
<code>starting</code>	a list with each tag corresponding to a parameter name. Valid tags are <code>alpha.1</code> , <code>alpha.2</code> , ..., <code>alpha.7</code> , and <code>sigma.sq</code> . The value portion of each tag is the parameter's starting value. See the Details for additional guidance on selecting starting values.
<code>tuning</code>	a list with each tag corresponding to a parameter name. Valid tags are <code>alpha.1</code> , <code>alpha.2</code> , ..., <code>alpha.7</code> , and <code>sigma.sq</code> . The value portion of each tag defines the variance of the Metropolis sampler Normal proposal distribution. Tuning values should be selected to keep the acceptance rate between approximately 20 and 50 percent.
<code>priors</code>	a list with tags <code>alpha</code> and <code>sigma.sq.IG</code> . <code>alpha</code> should be a list comprising <code>alpha.1.Unif</code> , <code>alpha.2.Unif</code> , ..., <code>alpha.7.Unif</code> with each of these tags set equal to a vector of length two that holds the lower and upper bound for the Uniform priors on the given <code>alpha</code> . The <code>sigma.sq.IG</code> is a vector of length two that holds the shape and scale parameters for the σ^2 's inverse-Gamma prior distribution. At minimum the <code>priors</code> list must include a prior for <code>sigma.sq.IG</code> . If α priors are not specified then they are assumed to follow their default values, see the Details section below.
<code>n.samples</code>	the number of MCMC samples to collect.
<code>sub.sample</code>	an optional list that specifies the subset of MCMC samples should be returned. Valid tags are <code>start</code> , <code>end</code> , and <code>thin</code> . The default values are <code>start=1</code> , <code>end=n.samples</code> and <code>thin=1</code> , i.e., no burn in or thinning.
<code>n.cores</code>	number of CPU cores to use for model fitting.
<code>eval.rast</code>	an optional TRUE/FALSE <code>RasterLayer</code> object indicating which pixels in <code>VI.rast</code> should be fit. TRUE signifies the model should be fit for the pixel and FALSE signifies it should not.

Details

Selection of the likelihood via the **family** argument should be respective of possible VI value range. The Beta likelihood assumes support for VI between 0 and 1. The Normal likelihood assumes support for VI on the whole real line. The default for the truncated Normal likelihood is support between 0 and 1; however, specifying the optional argument **t.normal.bounds** allows for user defined support bounds.

The default priors for the α 's are:

$$\begin{aligned}\alpha_1 &\sim \text{Unif}(\gamma_1, \gamma_2), & \alpha_2 &\sim \text{Unif}(0, \gamma_2 - \alpha_1), & \alpha_3 &\sim \text{Unif}(0, 1), \\ \alpha_4 &\sim \text{Unif}(0, \alpha_7), & \alpha_5 &\sim \text{Unif}(0, 0.001), & \alpha_6 &\sim \text{Unif}(0, 1), \\ \alpha_7 &\sim \text{Unif}(1, 365)\end{aligned}$$

The hyperparameters of these prior distributions can be changed using the **priors** argument.

An error will be thrown if an α starting value provided in the **starting** list is outside the default or supplied priors. Note, α_2 and α_4 have upper bounds determined by starting values of α_1 and α_7 , respectively.

Value

The output is a list of 9 **RasterBrick** objects. List components include:

alpha1.samps	is a RasterBrick holding the thinned post-burnin MCMC samples for α_1 at each evaluated pixel.
alpha2.samps	is a RasterBrick holding the thinned post-burnin MCMC samples for α_2 at each evaluated pixel.
alpha3.samps	is a RasterBrick holding the thinned post-burnin MCMC samples for α_3 at each evaluated pixel.
alpha4.samps	is a RasterBrick holding the thinned post-burnin MCMC samples for α_4 at each evaluated pixel.
alpha5.samps	is a RasterBrick holding the thinned post-burnin MCMC samples for α_5 at each evaluated pixel.
alpha6.samps	is a RasterBrick holding the thinned post-burnin MCMC samples for α_6 at each evaluated pixel.
alpha7.samps	is a RasterBrick holding the thinned post-burnin MCMC samples for α_7 at each evaluated pixel.
sigma2.samps	is a RasterBrick holding the thinned post-burnin MCMC samples for σ^2 at each evaluated pixel.
acc.rate	is a 2 band RasterBrick holding the overall Metropolis acceptance rate in the first band and the last batch acceptance rate in the second band (MH.acceptance output for pheno).

Author(s)

Chad Babcock <cbabcock@umn.edu>, Andrew O. Finley <finleya@msu.edu>